RICE UNIVERSITY

Quantum Shot Noise Characteristics in Atomic Scale Junctions at Liquid Nitrogen and Room Temperatures Using Novel Measurement Technique

by

Patrick J. Wheeler

A THESIS SUBMITTED
IN PARTIAL FULFILLMENT OF THE
REQUIREMENTS FOR THE DEGREE

Doctor of Philosophy

APPROVED, THESIS COMMITTEE:

Douglas Natelson, Chair
Professor of Physics and Astronomy and
Professor in Electrical and Computer
Engineering Fellow, Rice Quantum Institute

Emilia Morosan
Associate Professor in Physics and
Astronomy Associate Professor in Chemistry

Jason Hafner
Associate Professor in Physics and
Astronomy Associate Professor in Chemistry

Kevin Kelly
Associate Professor of Electrical and
Computer Engineering

Houston, Texas

January, 2014

ABSTRACT

Quantum Shot Noise Characteristics in Atomic Scale Junctions at Liquid Nitrogen and Room Temperatures Using Novel Measurement Technique

by

Patrick J. Wheeler

Shot noise encodes information not directly inferable from simple electronic transport measurements. Previous measurements in atomic-scale junctions have shown suppression of the shot noise at particular conductance values. This suppression shows that transport in these structures proceeds via discrete quantum channels. A novel measuring technique was used to probe these quantum shot noise characteristics at liquid nitrogen and room temperatures. This technique utilized high-frequency, broadband RF signal measurements of square-wave biased junctions and simultaneous extraction of shot noise power and conductance measurement data at high sampling rates. Junctions were created and measured at room temperature, utilizing both MCBJ and STM–BJ experimental design hardware. Noise suppression was observed at up to three conductance quanta in junction configuration ensembles, with possible indications of current-induced local heating and $1/f$ noise in the contact region at high biases. Lithographically created junctions were also measured, using the same electronics at liquid nitrogen temperature, enabling the examination of individual junction configurations. Nonlinearity and asymmetry were found in a significant number of the point contacts. Discrete changes were found in the bias dependence at threshold values of the bias, consistent with electronic excitation of local vibrational modes. Moreover, with

some regularity, significant mesoscopic variation in the magnitude of the noise was found in particular junctions, even with small changes in the accompanying conductance.

Pronounced asymmetries in the inferred noise magnitude were also observed as a function of bias polarity, suggesting current-driven ionic motion in the electrodes, even at biases well below those used for deliberate electromigration. These measurements demonstrate the quantum character of transport at room temperature at the atomic scale. This high-frequency broadband technique provides an additional tool for studying correlations in nanodevices.

Acknowledgments

To begin, I want to thank my advisor, Doug Natelson. His passion for and knowledge in Condensed Matter Physics are impressive. His guidance and advice through my time at Rice have been invaluable. I especially want to thank him for his encouragement, his trust and faith, his tremendous patience, and his recognition for the successes. Without Doug, I literally would not have successfully completed this program.

I also want to thank additional Committee members, Emilia Morosan, Jason Hafner, and Kevin Kelly. Your encouragement and advice during the program, participating in my PhD these defense, and providing followup recommendations is greatly appreciated.

Thank you to the present and past Natelson lab members. I have grown and benefited from each and every one of you.

I am deeply grateful to my family without whose support I would not have come this far. Many thanks to my parents who have been my lifelong continual cheer leaders and have always had my back. Thank you all for that you have done.

Contents

Abstract ii

Acknowledgments iv

List of Illustrations viii

1 Introduction and Background 1

1.1 Thesis Structure 1

1.2 Motivation 2

1.3 Types of Noise 4

1.3.1 $1/f$ Noise 5

1.3.2 Johnson-Nyquist Noise 6

1.3.3 Shot Noise 7

1.4 Landauer Model and Shot Noise: Theory–Debate–Resolution 9

1.4.1 Theory 9

1.4.2 Debate–Resolution 15

1.5 Mechanically Controlled Break Junction (MCBJ) 16

1.6 Historical Experimental Approaches and Designs 18

2 Experimental Design 20

2.1 Junction Formation Approaches Used in this Research 21

2.1.1 Mechanical Inchworm Actuator MCBJ 21

2.1.2 Piezo Actuator STM–BJ 23

2.1.3 Electromigrated Junctions 24

2.1.4 Comparison of Junction Formation Approaches 28

2.2 Novel Measurement Electronics 29

2.2.1 Low-Frequency Circuitry for Conductance Measurements 30
2.2.2 High-Frequency Circuitry for Shot Noise Measurements 32
2.2.2.1 Overview of High-Frequency Circuitry 32
2.2.2.2 Square-Wave Biasing of Junction 34
2.2.2.3 Determining Absolute Power with Logarithmic Power Inputs to the Lock-In 36
2.2.3 Electromagnetic Interference Mitigation 38

3 Calibration and Proof of Concept 41
3.1 Existing Methods 42
3.2 Simplified RF Equivalent Circuit of Vacuum Photodiode 43
3.3 Characteristic Impedance of Vacuum Photodiode 44
3.4 Calibration Methodology through Gain-Bandwidth Product 46
3.5 In Situ Measurements of Vacuum Photodiode – Proof of Concept 48
3.6 Characteristic Impedance of a Junction 49

4 Experimental Results 51
4.1 MCBJ Shot Noise Measurements at Room Temperature 51
4.1.1 Results and Analysis 51
4.1.2 MCBJ Summary 57
4.2 Electromigrated Junction Shot Noise Measurements at 77 K 59
4.2.1 Results and Analysis 59
4.2.2 Electromigrated Junction Summary 70

5 Summary Remarks and Future Directions 71

A Full MCBJ Electronic Circuit Diagram 73

B Full Photodiode Electronic Circuit Diagram 76

C Experimental Tips and Techniques **79**

Bibliography **82**

Illustrations

1.1 (a) shows a biased resistor R_S to produce $1/f$ noise; (b) is an example of $1/f$ voltage noise over time; (c) shows the frequency spectrum of the voltage squared. Adopted from [1]. 5

1.2 Johnson-Nyquist Noise: Left shows two white-noise voltage signals over time; the signal with the red markers has two times the voltage noise of the signal with the blue markers. Right shows constant power versus frequency for the same two signals. 6

1.3 The inter-arrival time of grains of sand through the neck of an hourglass is analogous to the shot noise of electrons in our nanojunctions. Adopted from [2]. 8

1.4 (a) A 1p39 vacuum photodiode [3]. (b) Plot of the shot noise produced by the 1p39 photodiode while in operation and illuminated. Adopted from [4]. 8

1.5 The Landauer free electron gas model illustrated as a system with two bulk wires connected by a constriction much smaller than the mean free path of the electron [5]. 10

1.6 Experimental diagram for producing a 2d electron gas and performing conduction measurements found in Figure 1.7 [6]. 11

1.7 The top section shows the conduction versus gate voltage. As the gate voltage increases, so does the width of the 2d electron gas. Suppression of the shot noise can be seen in the lower portion of the graph in approximate line with the plateaus in the conduction [6]. 11

1.8 Conduction channels opening, one by one, per Equation (1.5) [5]. 14

1.9 (a) Au conductance histogram. Adopted from [5]. (b) Potassium conductance histogram. Adopted from [5]. (c) Aluminum conductance histogram. Adopted from [7]. 15
1.10 (a) Van Ruitenbeek's design for measuring shot noise suppression in a break junction. (b) Solid dots are experimental from [8] while the solid and dashed lines are due to various levels of mixing of conductance channels as they open. An example can be found in Figure 1.8. 16
1.11 MCBJ design from [9]. 17
1.12 Rendition of a breaking metal point contact. 17
1.13 (a) A single molecule bridging the gap between a just-broken junction, allowing the molecule's conductance to be measured. (b) Molecular conductance peaks. (c) Dependence of conductance on molecular length. Adopted from [10]. 19

2.1 Mechanical actuator MCBJ where the relationship between U, T, L, Δx, and Δz can be found in Equation (2.1). 22
2.2 STM–BJ experimental design showing only the circuitry used for measuring the conductance. 23
2.3 SEM image of gold (Au) bowtie: rendition before electromigration on top; after electromigration, with junction formed, on bottom (gold-colorized for emphasis). 25
2.4 Shows two 3-axis piezo probes used to probe lithographically created devices at the bottom of an insertion stack [11]. 26
2.5 Shows an electromigrated Au bowtie break junction with typical dimensions. 27
2.6 Comparison chart of MCBJ, STM–BJ, and electromigrated junction formation approaches. 29

2.7 The low-frequency portion of the electronic design. The combined low-frequency and high-frequency circuit can be found in Figure 2.10. The total circuit with label explanation can be found in Appendix A.1. . . . 31

2.8 Where R_{gen} is the internal resistance of the function generator (Figure 2.7–K), R_{std} is the resistance of the resistance standard (Figure 2.7–H), R_{device} is the resistance of the junction (Figure 2.7–J), and R_{amp} is the internal resistance of the current pre-amplifier (Figure 2.7–I). See either Figure 2.7, the low-frequency diagram or Figure 2.10 for the full diagram (or Appendix A for the full diagram and annotation). 32

2.9 The high-frequency portion of the electronic design. The combined low-frequency and high-frequency circuit can be found in Figure 2.10. The total circuit with label explanations can be found in Appendix A. . . . 33

2.10 The complete electronic circuitry for the MCBJ, STM–BJ, and electromigrated junction experimental designs with both high and low-frequency portions of the circuit. The low-frequency portion of the circuit can be found in Figure 2.7, and the high-frequency portion in Figure 2.9. A full description of the diagram and components can be found in Appendix A. 34

2.11 Shows the power detector's logarithmic scale/calibration curve, the input power [dBm] on the X axis, and the corresponding output voltage [V] on the Y axis for Mini-Circuits ZX47-60+ power detector. The $PowerDetector^{-1}$ function's transfer curve used in Equation (2.5) is derived from this graph. 37

3.1 This diagram shows the high-frequency and low-frequency portions of the vacuum photodiode experimental design. A full description of the diagram and components can be found in Appendix B. 42

3.2 (a) Equivalent circuits for noise current sources. The sample itself has some short-circuit RMS current noise, i_s, and effective impedance, Z_s. Terminating one end of the sample with Z_0 results in a single-port equivalent circuit with RMS current noise i_g and impedance Z_g, as explained in Section 3.2. (b) Schematic of the reflection measurement relevant to determining the actual power transferred from the sample to the amplifier chain. 44

3.3 Schematics of circuits used to measure the RF reflection coefficient of the vacuum photodiode over the bandwidth of interest. The directional coupler has a coupling factor of -20 dB. The left circuit measures the reflected power at fixed frequency, and the spectrum analyzer's RF source is swept over 1000 discrete frequencies, ensuring all relevant features are captured. The right circuit measures the background noise power of the system. 45

3.4 (a) Schematic diagram showing design for measuring the gain-bandwidth product of the amplifier chain used in the experiments. The rest of the low-frequency circuit branch includes the resistance standard, current amplifier, and lock-in amplifier shown in Figure 2.7 and in the complete circuit diagram in Appendix A. (b) Schematic diagram showing circuit for background noise measurement in gain-bandwidth product configuration. . 46

3.5 (a) Measured gain versus frequency obtained using the circuit in Figure 3.4. (b) Fraction of power reflected by the vacuum photodiode as a function of frequency, obtained using the circuit in Figure 3.3. (c) Convolution of the gain-bandwidth product and $|\Gamma(\omega)|^2$, used to infer the photodiode current noise from the measured RF power, as described in the Section "Characteristic Impedance of Vacuum Photodiode" 3.3. 47

3.6 Current-voltage characteristics of the photodiode at three illumination levels (indicated by LED voltages) near the photodiode DC operating point of -45 V. Differential resistances at -45 V are indicated. 48

3.7 Shot noise [A^2/Hz] as a function of (square wave) current through the photodiode (tuned by various LED illumination intensities). The small offset indicates a small noise background and the slope is consistent with the expected $2eI$ to within three percent. This shows successful shot noise measurement for the photodiode and serves as a proof of concept for our measurement circuitry, calibration, and overall technique. 49

3.8 Schematic diagram for measuring the reflectance of the junction devices. Not shown are the rest of the low-frequency electronics hooked to the DC inputs of the bias tees, as in Figure 2.7, or in the full-circuit description in Appendix A. Inset graph: Reflectance versus G at 300 MHz. 50

4.1 Simultaneously acquired conductance histogram (upper curve, left axis) and averaged shot noise (lower curve, right axis). These data were taken at room temperature with V_{DC} = 100 mV, and square-wave frequency $\sim$1 kHz. 52

4.2 One choice of relevant transmission coefficients as a function of junction conductance. This is similar to the approach taken by van den Brom and van Ruitenbeek [8] (Figure 1.8). 53

4.3 Predicted current noise with no Nyquist-Johnson component, for (bottom to top) $V_{\mathrm{DC}} = 80$ mV, 100 mV, and 140 mV, calculated from Equation (4.1) using the transmission coefficient distribution shown in Figure 4.2 and recalling that V across the junction varies with G because of the series resistor. The vertical line shows the equivalent change in current noise expected at that conductance for a temperature change of 20 K. 54

4.4 Measured noise power as a function of conductance for (bottom to top) $V_{\rm DC} = 80$ mV, 100 mV, and 140 mV on a particular break junction, with no background subtraction. 55
4.5 Measured noise power as a function of DC bias current at two conductances. Dependence on the DC is slightly superlinear. Possible explanations for this are discussed in the text. 56
4.6 A scaled plot of normalized excess noise as a function of scaled bias for the junction in Figure 4.11. The linearity of this plot shows that the nonlinearity of around 0 volts in Figure 4.7 originates from the expected functional form of finite-temperature shot noise, as in Equation (4.1). 60
4.7 Inferred excess noise as a function of current in a junction with zero-bias resistance of 3 kΩ, showing intrinsic nonlinearity around 0 volts. 61
4.8 Examples of discrete changes in Fano factor at particular threshold voltage biases of tens of mV. Such changes in slope are consistent with previously reported observations [12] of inelastic electronic interactions with local vibrational modes, though in this case the junctions involve many conductance channels. The junction in this figure has a resistance of $600\ \Omega$. 62
4.9 Examples of discrete changes in Fano factor at particular threshold voltage biases of tens of mV. Such changes in slope are consistent with previously reported observations [12] of inelastic electronic interactions with local vibrational modes, though in this case the junctions involve many conductance channels. The junction in this figure has a resistance of 1.1 kΩ. 63
4.10 These figures show the relevant simultaneously acquired I as a function of V_{DC} data. These data do not show perceptible kinks at the voltages relevant for the changes in Fano factor, though this is not particularly surprising, given that lock-in techniques are generally necessary to resolve such features. 64

4.11 Noise asymmetry and mesoscopic sensitivity: Current as a function of time as V_{DC} is swept in a triangle wave between -200 mV and +200 mV, showing a stochastic transition between two junction configurations with similar conductances. Zero-bias resistance of the junction is 34 kΩ. 65

4.12 Noise asymmetry and mesoscopic sensitivity: the averaged, normalized excess noise as a function of scaled bias for the first configuration, showing two distinct branches, the upper branch with higher maximum noise corresponding to positive bias polarity. 66

4.13 Noise asymmetry and mesoscopic sensitivity: normalized excess noise as a function of scaled bias in the second configuration, with the upper branch again corresponding to positive bias polarity. 67

4.14 Noise asymmetry and mesoscopic sensitivity: the voltage and current of Figure 4.13 shows I as a function of V_{DC} before (open data marker) and after (filled data marker) the change in junction configuration. The change in noise asymmetry is considerably more dramatic. 68

4.15 Noise asymmetry and mesoscopic sensitivity: the raw lock-in measurement of the RF power detector as a function of time, showing clearly that the second junction configuration exhibits noise that is much more asymmetric in bias than the current itself in Figure 4.11. 69

A.1 Full MCBJ Electronic Circuit Diagram with detailed descriptions and part numbers. 75

B.1 Full Photodiode Electronic Circuit Diagram with detailed descriptions and part numbers. 78

Chapter 1

Introduction and Background

This thesis, "Quantum Shot Noise Characteristics in Atomic Scale Junctions at Liquid Nitrogen and Room Temperatures Using Novel Measurement Technique," introduces new experimental approaches and techniques that probe many-body electron systems and measures electron–electron correlation through shot noise measurements. The following section lays out the structure of the thesis.

1.1 Thesis Structure

- Chapter 1 provides the motivation and background for this research, introduces two interfering noise sources ($1/f$ and Johnson-Nyquist), and shot noise (the signal of interest), followed by the connection of shot noise with conductance channels through the Landauer model, and some historical background on prior experiments.
- Chapter 2 covers the experimental designs (MCBJ, STM–BJ, and electromigrated junction), the novel measurement circuitry leveraged across all three designs, and electromagnetic interference mitigation strategies.
- Chapter 3 covers the calibration and proof of concept of the new approaches and techniques, using a reference vacuum photodiode to validate and verify the experimental design to both ourselves and critics.

- Chapter 4 builds on the preceding foundation with experimental results. Measurements were taken of configuration-ensemble averages at room temperature as well as individual configurations at liquid nitrogen temperature.
- Chapter 5 provides a summary and forward-looking comments.
- Appendices A, B, and C provide supplementary material.

1.2 Motivation

An amazing property of nature is that, as additional physical elements are added to a system, new properties, such as superconductivity, superfluidity, quasiparticles, and quantum phase transitions, can emerge, as P.W. Anderson postulated in his 1972 article, "More Is Different" [13]:

> "...at each new level of complexity, entirely new properties appear, and the understanding of these behaviors requires research which I think is as fundamental in its nature as any other."

Anderson succinctly describes how it has not been possible to understand "many-body" systems by just applying the "few particle" principles. The article reinforces this line of thought:

> "The ability to reduce everything to simple fundamental laws does not imply the ability to start from those laws and reconstruct the universe."

It is perhaps more accurate, and definitely more practical, to assert that it is possible to reconstruct the universe from fundamental laws if the scope of those laws includes those derived from the unique behaviors observed in many-body systems. The study of fundamental laws observable only under these many-body conditions in solids and liquids has

come to be called condensed matter physics. Just as particle physics uses high energy and astrophysics uses telescopes, many-bodied systems are the lens through which condensed matter physicists probe reality.

The physics of condensed matter focuses primarily on many-body systems impossible to study from the few particle principles. Take, for example, the many-electron Hamiltonian:

$$H_e = \sum \frac{p_i^2}{2m} + \frac{1}{2}\sum_{i \neq j} \frac{e^2}{|r_i - r_j|} + U(\vec{\mathbf{r}}) \tag{1.1}$$

Because of the N^2 number of electron–electron interaction terms in the Hamiltonian, and the fermionic character of electrons, modeling systems from the few particle principles is usually unfeasible due to the sheer number of terms as the system approaches mesoscopic scales, let alone macroscopic scales.

Although using exact few particle principles is often not viable, in many cases simple models based on approximations or simplifications can yield results that correlate well with observations of relevant physical properties. One example of this simplified modeling is the free electron gas model of a metal conductor. This model was developed and first presented by Sommerfield at the Como Conference as documented by Hoddeson [14] and first formalized in the paper "Zur Elektronentheorie der Metalle" [15]. The primary assumptions of the free electron gas model are:

- The electrons treat the boundary of the box as an infinite potential barrier.
- The electrons do not interact, other than through Fermi-Dirac statistics.
- The electrons follow Fermi-Dirac statistics.

With these simplifications, this model of the electrons parallels the model of an ideal gas in a box. Since the electrons are only correlated because of Fermi-Dirac statistics, the

total solution is merely a linear combination of anti-symmetrized single-particle solutions. Despite the simplicity of the free electron gas model, the Fermi-Dirac statistics ensure it correlates well with observed reality, giving insight into several properties of bulk conductors, including conductivity and the temperature dependence of the heat capacity.

When exploring new physical systems, this uncorrelated electron model is often a good starting point; however, there are many physical systems where this simplified model will neither match experimental observations nor provide the desired insights. It is often necessary to consider how the electrons interact and influence each other, i.e., how the electrons are correlated in time and space. In such cases, it falls to experimental investigation to explore and probe the many-body systems for more information and insights. The results help develop new or more accurate models and codify new fundamental laws.

1.3 Types of Noise

When measuring a small electrical current, taking a photograph, or trying to understand a conversation in a busy restaurant, noise is often thought of as a randomly varying background signal that interferes with a desired signal. A considerable amount of thought and energy goes into eliminating or at least reducing such background noise. In many physical phenomena, however, while the background noise is random, it is limited or shaped in ways that can give insight to underlying physical properties. An example that is considered to be the founding moment of noise as a field of study is Richard Brown's observation in 1827 [16] that pollen particles suspended in water had an unexplained random or noisy motion. Though not the first observation of what is now know as "Brownian motion," Brown's observations, formalized by Albert Einstein in 1905 [17], were instrumental in confirming the existence of molecules, all because of the noisy movements of pollen suspended in water. Using noise to reveal such underlying insights is just one of the tools

available to researchers in condensed matter. Shot noise, in particular, as described below in Section 1.3.3, is a tool that provides insights into quantum conductance channels and electron–electron interactions. Measuring shot noise can be difficult due to interference from other types of noise. The subsections below provide background on $1/f$ noise, Johnson-Nyquist noise, and shot noise.

1.3.1 $1/f$ Noise

Flicker, $1/f$, or pink noise, is ubiquitous and found in everything from electrical measurements to the rotation of the earth, yet its exact origin varies from system to system. It was first reported by Johnson [18] as a phenomena similar to what is now called Johnson noise [19]. It can even be found in the pitch and rhythm of classical music [20]. No-

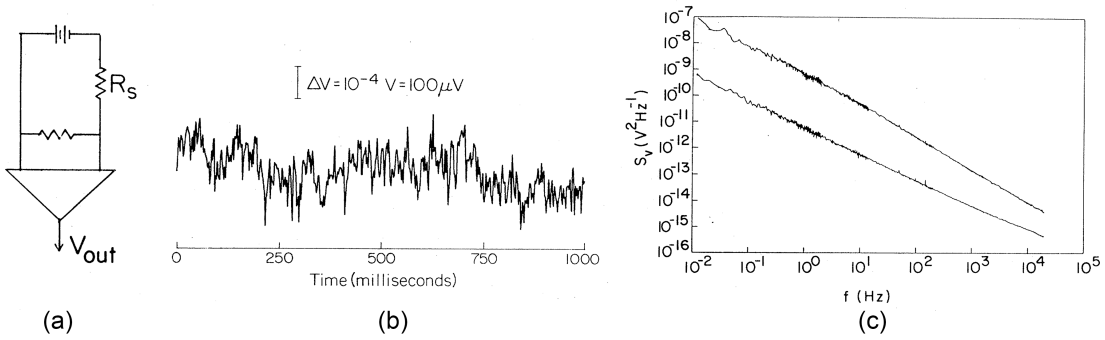

Figure 1.1: (a) shows a biased resistor R_S to produce $1/f$ noise; (b) is an example of $1/f$ voltage noise over time; (c) shows the frequency spectrum of the voltage squared. Adopted from [1].

tably, $1/f$ noise causes problems in many low-frequency electrical measurements. The exact origin of flicker noise is diverse and unknown in particular systems [1]. In many solid-state systems, including nanoscale junctions, it is believed to be caused by small shifts in atoms or ions [1]. Fortunately, with its inverse relationship with frequency, $1/f$

noise dies off quickly by shifting measurements to higher frequencies and it is often possible to minimize or avoid $1/f$ noise effects altogether, as done in this thesis. For more discussion of $1/f$ noise in nanoscale junctions, see [21].

1.3.2 Johnson-Nyquist Noise

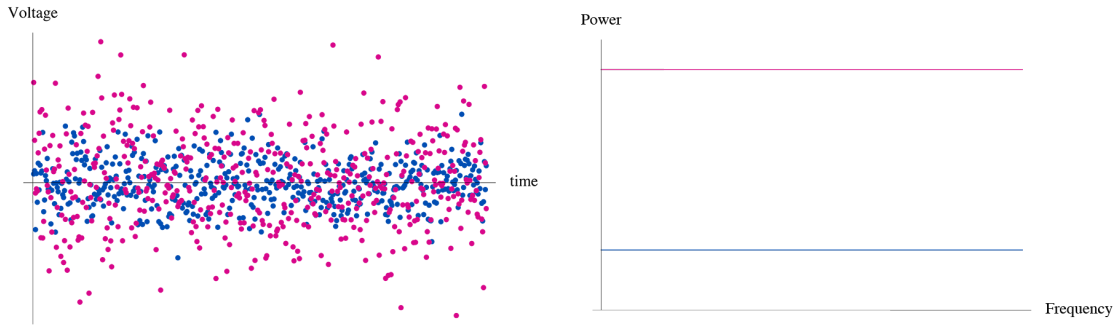

Figure 1.2: Johnson-Nyquist Noise: Left shows two white-noise voltage signals over time; the signal with the red markers has two times the voltage noise of the signal with the blue markers. Right shows constant power versus frequency for the same two signals.

One common electronic noise source in conductors is Johnson-Nyquist noise. Discovered by Johnson and formalized by Nyquist in 1928, at Bell Labs [22], this noise is the result of small, random voltage fluctuations caused by the thermally driven fluctuations of electrons in the conductor. Unlike shot noise, Johnson-Nyquist noise is present when the system is in thermodynamic equilibrium. Johnson-Nyquist noise is analogous to blackbody radiation, where the noise power spectrum is white up to the quantum cutoff, and is a consequence of the fluctuation-dissipation theorem [23].

This noise spectrum with the quantum cutoff can be easily simulated with an RCL-equivalent circuit with an ideal resistor used as the noise generator. Well below the cutoff

frequency, the expected voltage noise power (mean square voltage fluctuations) within a bandwidth Δf is given by:

$$S_v = \overline{V^2} - \overline{V}^2 = 4k_B T R \Delta f \tag{1.2}$$

Although this Johnson-Nyquist noise was originally measured for $\overline{V^2}$ versus T, it is often more helpful to think of the noise as power instead of $\overline{V^2}$ in the following form:

$$P = \frac{S_v}{R} = 4k_B T \Delta f \tag{1.3}$$

Thinking of the noise in terms of power makes it clear that the total power is invariant for changes in voltage and only varies for changes in temperature or bandwidth.

1.3.3 Shot Noise

Shot noise is another type of electronic noise that originates in the discrete nature of electric charge. It is found only when the system is out of thermodynamic equilibrium, most often from a driving voltage in an experimental design. A helpful analogy in understanding the discrete particle source of shot noise is to envision an hourglass on its side, with the upper glass bulb filled with sand (Figure 1.3). Then consider the hourglass being slightly lifted toward the upright position until individual grains of sand are barely falling through the neck of the hourglass, one at a time. The grains of sand do not arrive in the lower glass bulb at even intervals, but, rather, with great variation in each grain's inter-arrival time. That variation in inter-arrival time of each grain of sand is an example of shot noise. If you equate the grains of sand with discrete electronic charges, and the hourglass with the junction of a metal point contact, then electronic shot noise is equivalent to the variation in the mean inter-arrival time of charge carriers across the junction of the metal point contact.

Figure 1.3: The inter-arrival time of grains of sand through the neck of an hourglass is analogous to the shot noise of electrons in our nanojunctions. Adopted from [2].

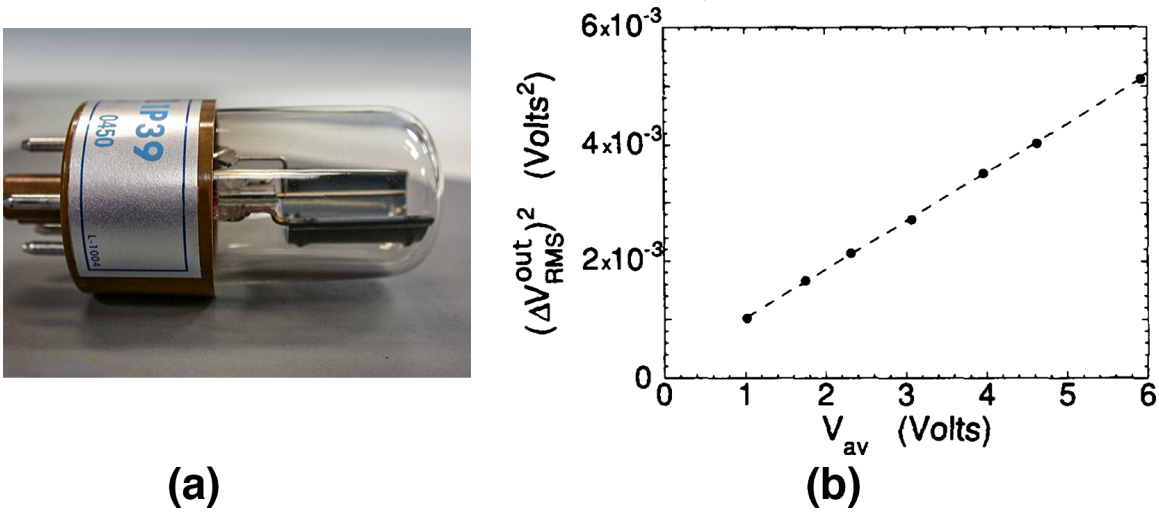

Figure 1.4: (a) A 1p39 vacuum photodiode [3]. (b) Plot of the shot noise produced by the 1p39 photodiode while in operation and illuminated. Adopted from [4].

Shot noise in electronics was discovered by Schottky, in 1918, [24] using vacuum pho-

todiodes, as seen in Figure 1.4-(a). In shot noise, the mean square current noise per Hz is related to I, the average DC as $S_I = F \cdot 2eI$, as can be seen in Figure 1.4-(b). Here, e is the electronic charge and F is the Fano factor. In the classical case, where it is assumed all electrons are uncorrelated, in the Poissonian limit, $F = 1$. This classical Fano factor can be altered by quantum transport process, some of which can be explained by the Landauer model.

1.4 Landauer Model and Shot Noise: Theory–Debate–Resolution

1.4.1 Theory

The Landauer, or scattering, model can be thought of as the application of the gas model, mentioned above in Section 1.2, to a system with two bulk wires connected by a constriction much smaller than the mean free path of the electron (Figure 1.5). If we considered the two wires loosely coupled via the constriction represented by a transmission matrix t, then we can think of each wire as a mostly independent electron gas system with standing plane waves in the vertical direction, and the waves we would normally consider relevant to conduction in the horizontal direction. With this assumed Landauer model and quantum transmission matrix as t, the conductance is in the linear regime [5]:

$$G = \frac{2e^2}{h} Tr(t^\dagger t) \tag{1.4}$$

where Tr is the trace operator. Given the assumptions of the Landauer model, it is always possible to change the wave basis to one in which $t^\dagger t$ is diagonal, with diagonal matrix

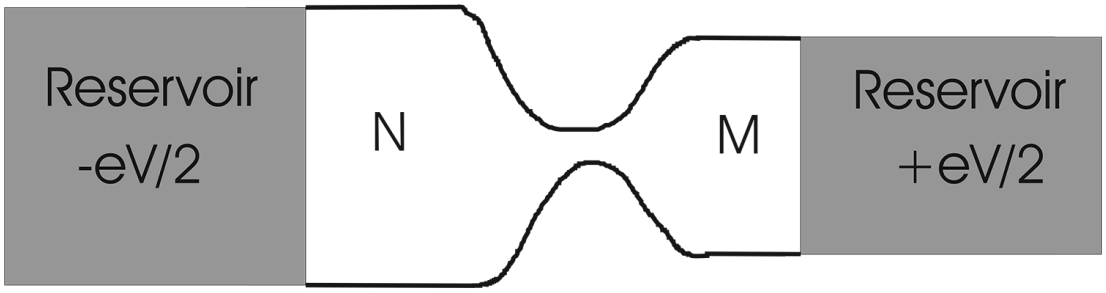

Figure 1.5: The Landauer free electron gas model illustrated as a system with two bulk wires connected by a constriction much smaller than the mean free path of the electron [5].

elements τ_i corresponding to the transmission probability of each channel:

$$G = \frac{2e^2}{h} \sum_{i=1}^{Nc} \tau_i \tag{1.5}$$

where $\tau_i = |t_{ii}|^2$. It is common to refer to each τ_i as a conduction channel.

These conduction channels were first explored in [25, 26, 27] through measurements of conductance quantization, and later explored in terms of shot noise in ground-breaking work by Reznikov and Kumar with semiconductor quantum point contacts in [6, 28]. In the referenced work, a semiconductor device, controlled by gating, produced a 2d electron gas, where the width of the 2d electron gas determined the number of 1d conduction channels, as in Equation (1.5). The design for the point contact can be seen in Figure 1.6. As seen in Figure 1.7, as the gate voltage increases, the effective width of the 2d electron gas increases, and the conduction is observed to change in a step-like manner, with each step of $\Delta G = \frac{2e^2}{h}$ corresponding to the opening of an additional transmitting channel. In the figure's lower panel, the shot noise can be seen to be suppressed during the conductance plateaus.

As mentioned in Section 1.3.3, the shot noise in photodiodes and other classical devices is found to be $S_I = F \cdot 2eI$. At low temperature, the shot noise in the Landauer model is

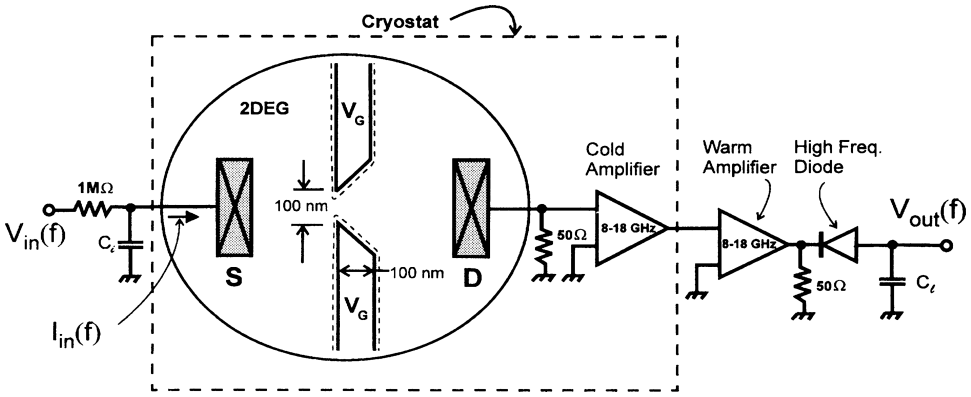

Figure 1.6: Experimental diagram for producing a 2d electron gas and performing conduction measurements found in Figure 1.7 [6].

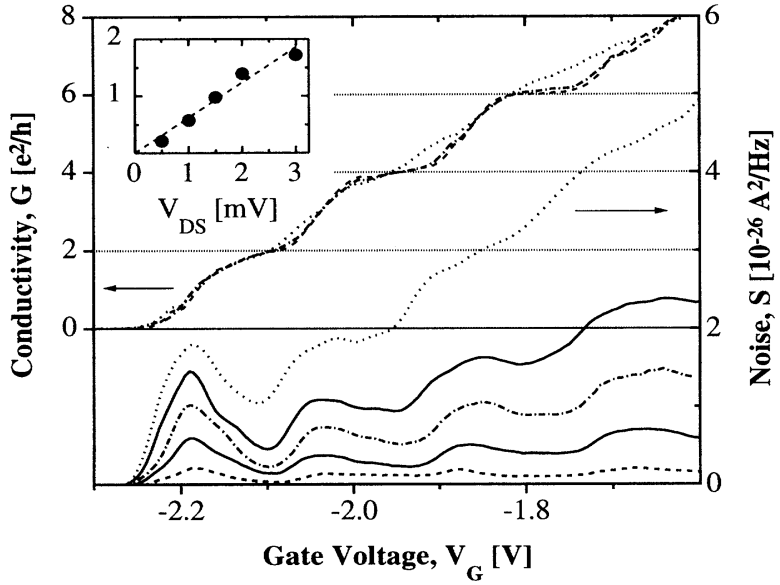

Figure 1.7: The top section shows the conduction versus gate voltage. As the gate voltage increases, so does the width of the 2d electron gas. Suppression of the shot noise can be seen in the lower portion of the graph in approximate line with the plateaus in the conduction [6].

modified to be [25, 29]:

$$P_I = 2eVG_0 \sum_i \tau_i(1-\tau_i) = \frac{2e^3V}{h} \sum_i \tau_i(1-\tau_i) \tag{1.6}$$

where τ_i is the same transmission channel found in Equation (1.5). Insights into the meaning of the $\tau_i(1-\tau_i)$ term can be had by examining the derivation of partition noise, which has a comparable term. Consider a beam of particles with intensity $\langle n \rangle = 1$ incident on a probabilistic barrier. Each particle interacting with the barrier is either transmitted with probability T or reflected with probability R. Thus, the transmitted intensity is $\langle n_T \rangle = T$ and the reflected intensity is $\langle n_R \rangle = R$. The mean squared fluctuation is $(\Delta n_T)^2 = (n_T - \langle n_T \rangle)^2$ and $(\Delta n_R)^2 = (n_R - \langle n_R \rangle)^2$. Given that a positive fluctuation in transmit ion intensity is a negative fluctuation in the reflection intensity:

$$\begin{aligned} \Delta n_T &= n_T - \langle n_T \rangle \\ &= (1 - n_R) - (1 - \langle n_R \rangle) \\ &= -(n_R - \langle n_R \rangle) \\ &= -\Delta n_R \end{aligned} \tag{1.7}$$

we have:

$$\left\langle (\Delta n_T)^2 \right\rangle = \left\langle (\Delta n_R)^2 \right\rangle = -\left\langle \Delta n_T \Delta n_R \right\rangle \tag{1.8}$$

and this simplifies to:

$$\begin{aligned}
\left\langle (\Delta n_T)^2 \right\rangle &= -\left\langle \Delta n_T \Delta n_R \right\rangle \\
&= -\left\langle (n_T - \langle n_T \rangle)(n_R - \langle n_R \rangle) \right\rangle \\
&= -\left\langle n_T n_R - n_T \langle n_R \rangle - n_R \langle n_T \rangle + \langle n_T \rangle \langle n_R \rangle \right\rangle \\
&= -(\langle n_T n_R \rangle - 2 \langle n_T \rangle \langle n_R \rangle + \langle n_T \rangle \langle n_R \rangle) \\
&= \langle n_T \rangle \langle n_R \rangle \; since \; n_T n_R \; must \; equal \; zero \\
&= TR \\
\left\langle (\Delta n_T)^2 \right\rangle &= T(1-T)
\end{aligned} \tag{1.9}$$

This demonstrates the relationship between the transmission probability and the τ_i found in the Landauer model.

The Fano factor is a quick and convenient method of quantifying the difference between a model, or experiment, and classical shot noise. The Fano factor for the low-temperature Landauer model is simply the Landauer shot noise divided by the classical shot noise:

$$F = \frac{2eVG_0 \sum_i \tau_i(1-\tau_i)}{2eI} = \frac{2eVG_0 \sum_i \tau_i(1-\tau_i)}{2eVG_0 \sum_i \tau_i} = \frac{\sum_i \tau_i(1-\tau_i)}{\sum_i \tau_i} \tag{1.10}$$

It is the $\tau_i(1-\tau_i)$ term that produces shot noise suppression in an ideal single channel device. In this single-channel system, the shot noise can be suppressed to zero when either the channel is fully transmitting, $\tau_i = 1$, or when fully closed, $\tau_i = 0$. Most systems found in nature, however, will not be ideal or single-channel, so shot noise suppression will only be partial, given all channels are unlikely to be exactly closed or open. Alkali and other monovalent metals, at low temperature, are convenient for the study of shot noise suppression. When two pieces of such metals are brought together, a constriction is formed,

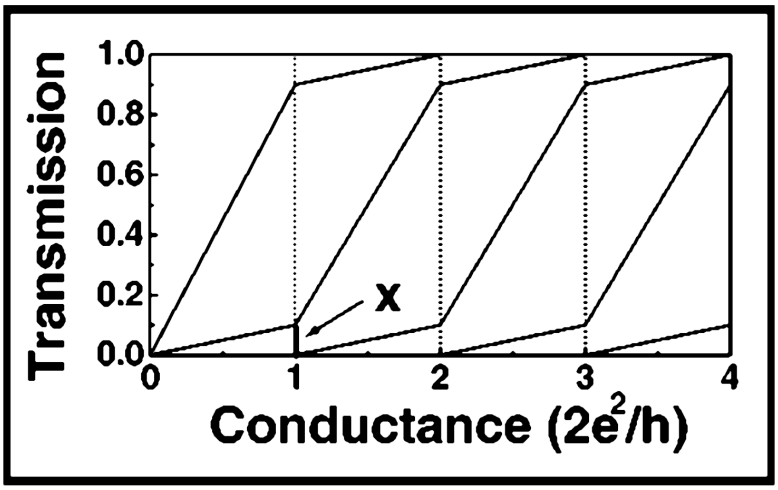

Figure 1.8: Conduction channels opening, one by one, per Equation (1.5) [5].

which increases in the cross-sectional area. With these metals, there is a tendency for one conduction channel to open completely before the next starts to open (Figure 1.8), leading to a high degree of shot noise suppression [5].

The picture becomes slightly more complicated with the addition of finite temperature, even while assuming only elastic collision effects [25]:

$$S_I = 4k_{\rm B}TG_0 \sum_i \tau_i^2 + 2eV \coth \frac{eV}{2k_{\rm B}T} G_0 \sum_i \tau_i(1-\tau_i). \tag{1.11}$$

The two terms combine to give Johnson noise in the limit that V $\to$ 0. This is expected to be valid at frequencies much smaller than $k_{\rm B}T/\hbar$ and $eV/\hbar$, and voltages smaller than the characteristic energy scales over which the τ_i vary. As seen from Eq. (1.11), in the limit of a small number of channels opening one by one, strong suppression of shot noise is expected when channels are fully transmitting ($\tau_i \to 1$). Shot noise is further suppressed in macroscopic conductors because of inelastic electron-phonon scattering, which effectively "smears" electrons across various channels [25].

1.4.2 Debate–Resolution

Nanoscale metallic junctions are great tools for the condensed matter physicist. A well-known technique is to measure the conduction while breaking and forming the junction and to histogram the data. In many metals, peaks often appear near $(2e^2)/h$, the conductance quanta. Examples of such conductance histograms can be seen in Figure 1.9. Early on in this type of experimentation and data gathering, there was a healthy debate over whether the conductance peaks actually represented a quantum phenomenon. Confounding the problem is the fact that many conduction peaks in metals are tantalizingly similar in conductance, suggesting a quantized nature, while other metal conductance histograms seem to break the model. Some inferred that this meant it was mere chance that some peaks lined up with $(2e^2)/h$ (Figure 1.9). Rubio's data, showing that changes in conductance were not coupled to changes in force by using an AFM while taking conductance traces in [30], presented the first convincing evidence that conductance peaks were not atomic scale rearrangements [31].

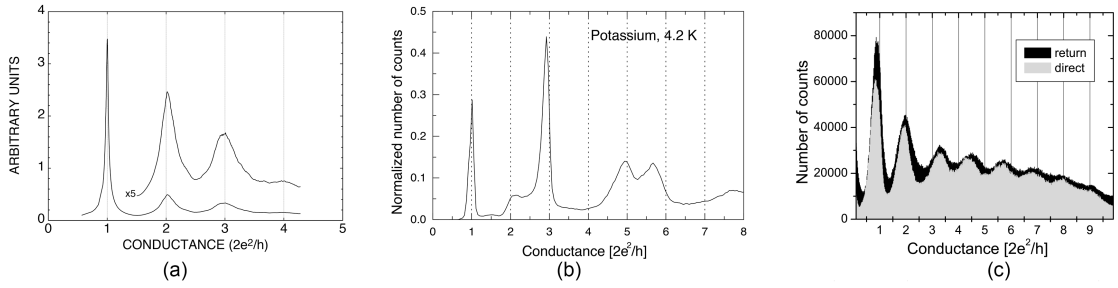

Figure 1.9: (a) Au conductance histogram. Adopted from [5]. (b) Potassium conductance histogram. Adopted from [5]. (c) Aluminum conductance histogram. Adopted from [7].

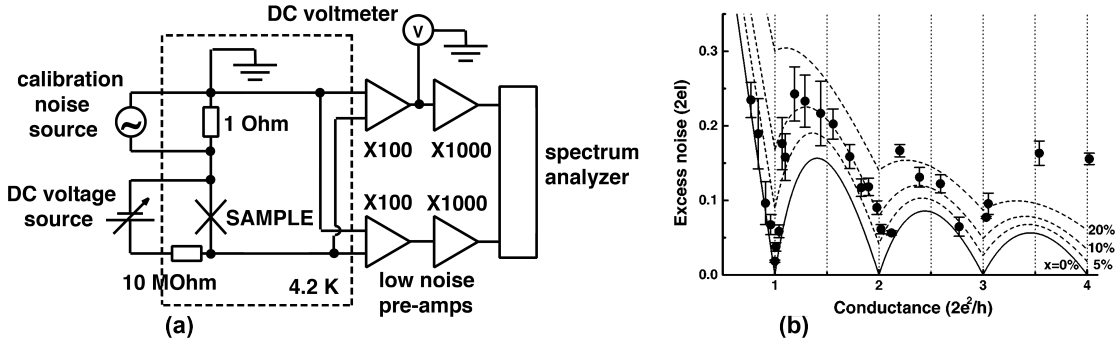

Figure 1.10: (a) Van Ruitenbeek's design for measuring shot noise suppression in a break junction. (b) Solid dots are experimental from [8] while the solid and dashed lines are due to various levels of mixing of conductance channels as they open. An example can be found in Figure 1.8.

1.5 Mechanically Controlled Break Junction (MCBJ)

To create the atomic junction, the mechanically controlled break junction (MCBJ) is used to place two metal surfaces in physical contact, and then slowly retract the surfaces from each other. Figure 1.11 shows a stereotypical MCBJ from van Ruitenbeek's 1996 paper [9]. At this atomic scale, most metals are ductile, so, as one surface is retracted from the other, a metal nanowire is formed (Figure 1.12). As extension continues, the nanowire stretches, narrows, and eventually breaks. The metal surfaces are then contracted back together, where the junction formation process begins again.

Mechanical break junctions have proven to be a valuable tool in understanding the physics of electronic conduction in metals at the atomic scale [31, 32, 33]. By bringing two metals in and out of contact while simultaneously performing electrical measurements, it is possible to build up a histogram of conductance values that occur when the contact between the electrodes ranges from tunneling to the few-atom level. In metals with s-like conduction electrons, well-defined peaks in conductance histograms near integer multiples

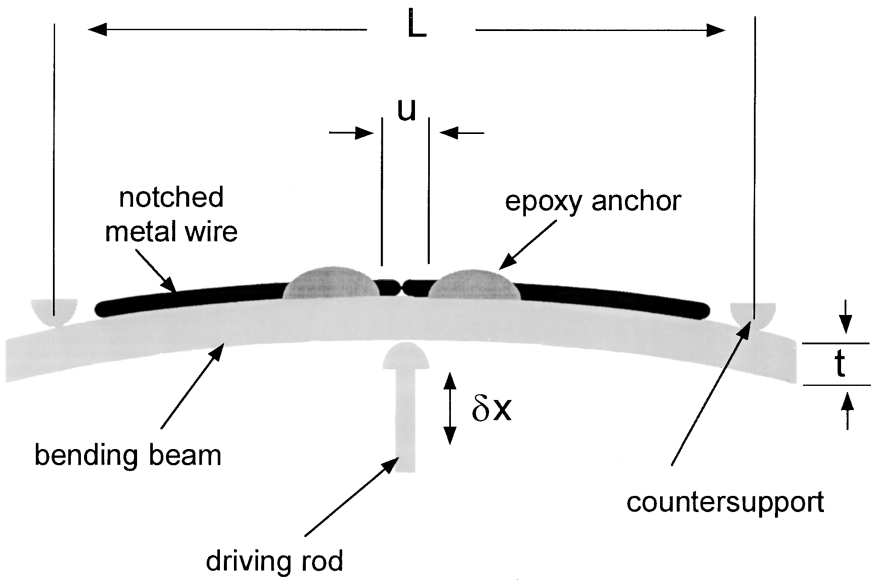

Figure 1.11: MCBJ design from [9].

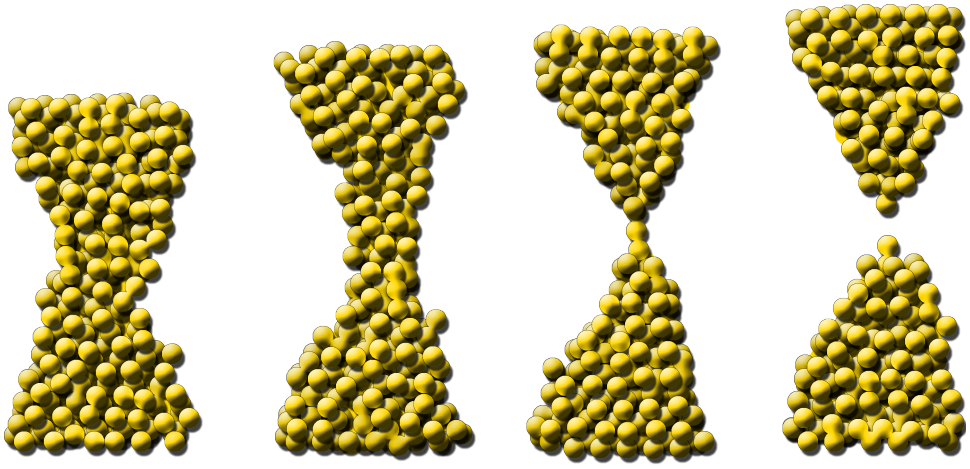

Figure 1.12: Rendition of a breaking metal point contact.

of the quantum of conductance ($G_0 \equiv 2e^2/h$) frequently appear. These are now interpreted as a signature of conductance quantization, transport of electrons through an integer number of transmitting quantum channels.

1.6 Historical Experimental Approaches and Designs

From the conductance and conductance histograms discussed in Section 1.5 alone, it is generally not possible to determine whether particular peaks in conductance histograms are the result of quantized electronic transport through well-defined quantum channels or whether these peaks merely indicate particularly stable junction configurations.

The mapping of conductance into transmission coefficients for discrete quantum electronic channels requires additional information beyond the linear conductance. Two approaches have been pursued at cryogenic temperatures to infer the quantum nature of conduction in such junctions. Sub-gap structure in superconducting point contacts [34] is one means of identifying the number of transmitting channels and their particular transmission coefficients. Alternately, shot noise, (Section 1.3.3), may be used to examine the same physics.

The break junction approach has recently been extended to examine ensemble-averaged conduction in single-molecule junctions as seen in Figure 1.13-(a) [35, 36, 37]. The ability to acquire such histograms at room temperature at relatively high rates has greatly advanced studies of molecular conduction, permitting systematic studies of the effects of contact functionalization [38, 39], molecular conformation as shown in Figure 1.13-(b) [10, 37], and molecular length as seen in Figure 1.13-(c) [37].

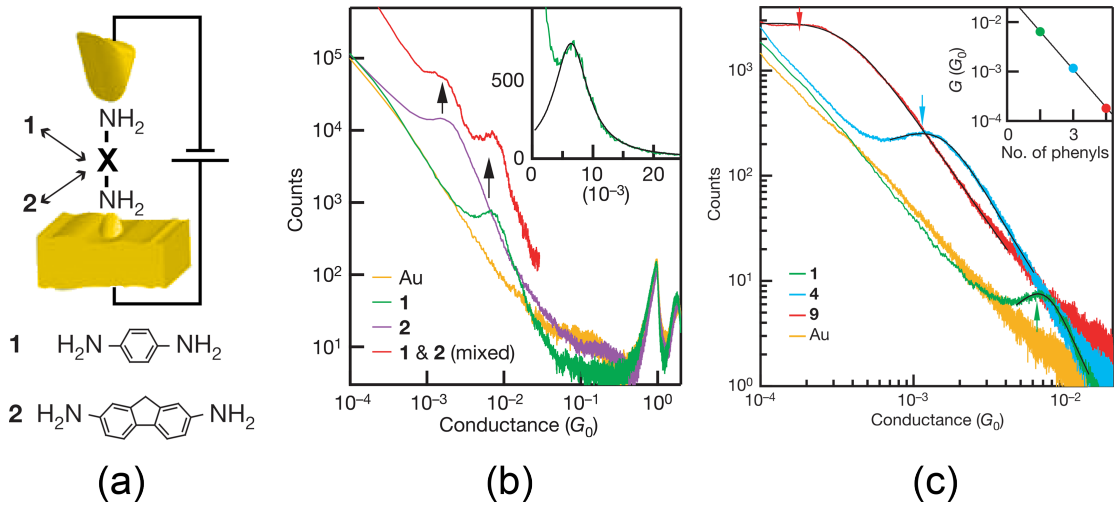

Figure 1.13: (a) A single molecule bridging the gap between a just-broken junction, allowing the molecule's conductance to be measured. (b) Molecular conductance peaks. (c) Dependence of conductance on molecular length. Adopted from [10].

Chapter 2

Experimental Design

Atomic scale junctions are a challenge to create and measure. These junctions have active regions just tens of nanometers in extent, yet the average physical vibrations in an office environment are 10,000 times that magnitude [40]. The electrical power being measured in these experiments is around 10^{-16} watts, although the average signal power from a local cell phone can be in the order of watts. All of these physical and electromagnetic random noise sources present substantial difficulties in creating a stable, reliable, repeatable, and productive experimental design. The mechanics of atomic scale junctions are fragile and subject to the smallest vibrations. Any stray electromagnetic signal from, for example, local equipment, local cell phones, or even distant radio stations is extrinsic noise that could mask any useful signal from the junction. These challenges are increased when measurements are taken at room temperature, where junction stability is reduced and naturally occurring noise sources in the materials are more active. The experimental designs used in this research help mitigate many of these challenges to ensure the experimental measurements are meaningful in the midst of a natural environment with high mechanical and electrical noise.

This chapter covers the physical description, the measurement electronics, and the EMI mitigation strategy of the three experimental designs used in this research.

2.1 Junction Formation Approaches Used in this Research

This section covers the three experimental mechanisms used in this research to form junctions:

1. Mechanical inchworm actuator MCBJ (Figure 2.1)
2. Scanning tunneling style break junction (STM–BJ) (Figure 2.2)
3. Electromigrated junction (Figure 2.3)

This is followed by a short section with a side-by-side comparison of the three junction creation approaches.

2.1.1 Mechanical Inchworm Actuator MCBJ

The first approach used to create a junction for this research utilized a mechanical inchworm actuator MCBJ, as seen in Figure 2.1. It uses a notched Au wire mounted on, and electrically isolated from, a flexible metal shim. The notch in the Au wire determines where the Au wire will break, forming the two Au electrodes with opposing surfaces on the first extension cycle.

To electrically measure the characteristics of the junction, the signal lines of two coaxial cables are connected to either end of the Au wire. The ground connection of the coaxial cables are connected to opposing sides of the shim to increase signal integrity by reducing external RF interference. A computer-controlled inchworm motor pushes and retracts the actuator arm to flex the shim, which bring the ends of the Au wire (electrodes) repeatedly in and out of contact.

The Au electrode's movements are directly coupled, yet orthogonal, to the movement of the inchworm actuator arm, only greatly attenuated. The attenuation factor can be cal-

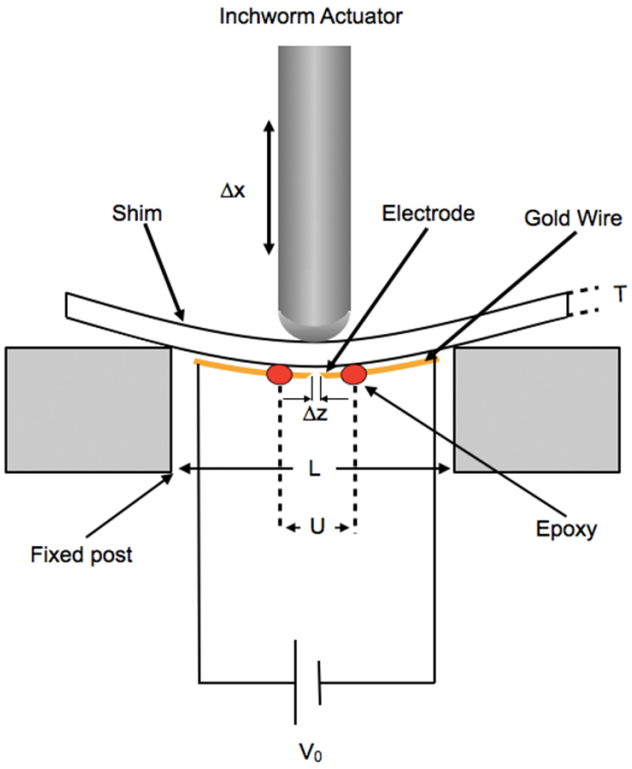

Figure 2.1: Mechanical actuator MCBJ where the relationship between U, T, L, Δx, and Δz can be found in Equation (2.1).

culated with Equation (2.1) from [9]. This allows extremely fine control of position and smooth slow electrode movement, Δz,

$$\Delta z = \frac{6UT}{L^2}\Delta x \tag{2.1}$$

where U is the distance between the epoxy spots holding the electrodes, T is the thickness of the shim, and L is the distance between the fixed posts, as seen in Figure 2.1.

This mechanical inchworm actuator MCBJ suffered from several deficiencies:

- Physical constraints of the inchworm actuator limited junction formation to just tens of cycles per minute.

- Properly mounting and notching the Au wire had a low success rate.
- Difficult sample preparation—breaking the initially notched Au wire to form the junction did not have a high success rate. It was also difficult to keep the junction clean during sample creation, a prerequisite for reliable data collection.
- RF properties of the Au wire and electrodes differed from sample to sample because of the variability in the spacing from the Au wire/electrodes to the shim, the geometry of the shims, and placement of the coaxial ground path on the shim.

2.1.2 Piezo Actuator STM–BJ

To overcome the limitations of the inchworm actuator MCBJ of the above Section 2.1.1, a scanning tunneling microscope-style break junction (STM–BJ) was designed and used to create junctions (Figure 2.2). The Au tip of the STM–BJ is directly controlled by a stack of piezos for highly repeatable movement. Although the surrounding test equipment, mea-

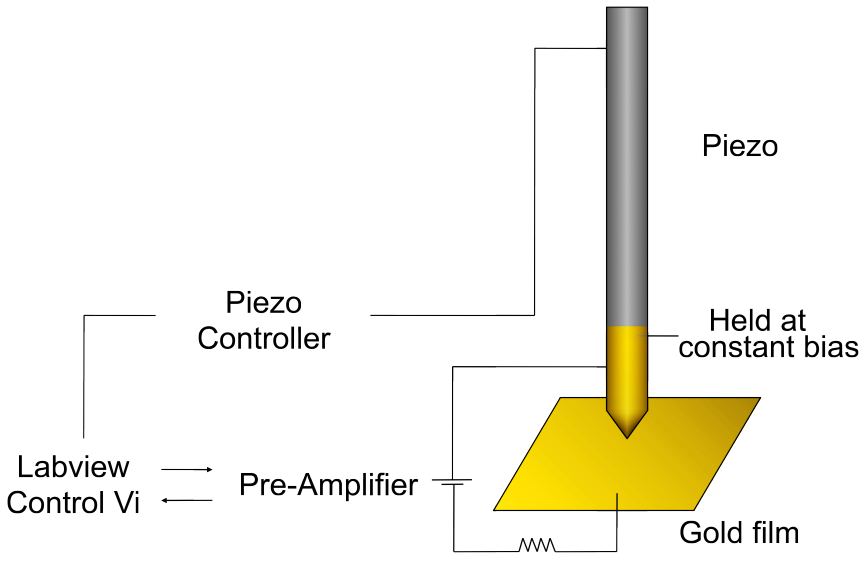

Figure 2.2: STM–BJ experimental design showing only the circuitry used for measuring the conductance.

surement circuitry, and data analysis approach are all the same as the inchworm actuator MCBJ design in the above Section 2.1.1, the STM–BJ approach is substantially different. Compared with the inchworm-actuated MCBJ, the STM–BJ possesses some key advantages, with few deficiencies:

- The junction is formed between a Au film and a Au point attached directly to the actuator. This direct and simple geometry is easier to construct.
- The actuator is controlled by a piezo (piezo crystal/crystal stack) which allows fine and accurate positional control.
- The piezo allows rapid and accurate control of the actuator movement, resulting in a junction cycling rate more than ten times that of the inchworm actuator MCBJ.
- Sample preparation consists of merely ensuring a fresh layer of Au for the surface and tip. For the Au film surface, this is the deposition of a freshly evaporated metal layer. The tip is cleaned by cutting the old surface away. In a leveraged use of this STM–BJ, Ruoyu Chen, in [41], found that annealing the Au junction with high currents is a more convenient method of sample cleaning.
- The consistent geometry of the STM–BJ junction provided more stable RF properties, including repeatable impedance.

The primary disadvantage of this STM–BJ is that the vibrations along the piezo actuator axis are not scaled down, as is the case with the inchworm actuator MCBJ. This makes the STM–BJ more sensitive to vibration.

2.1.3 Electromigrated Junctions

Electromigrating, lithographically created gold (Au) “bowtie” junctions, as shown be-

low in Figure 2.3, is the third approach to creating junctions in this research. A ramping bias is applied to the Au bowtie from 0 to between 0.3 and 0.9 volts under a feedback-controlled electromigration process, with the junction resistance determining the maximum ramp voltage. Once a desired resistance level is reached, indicating the junction has been formed, the electromigration process is halted. Electromigration is the process of electrons

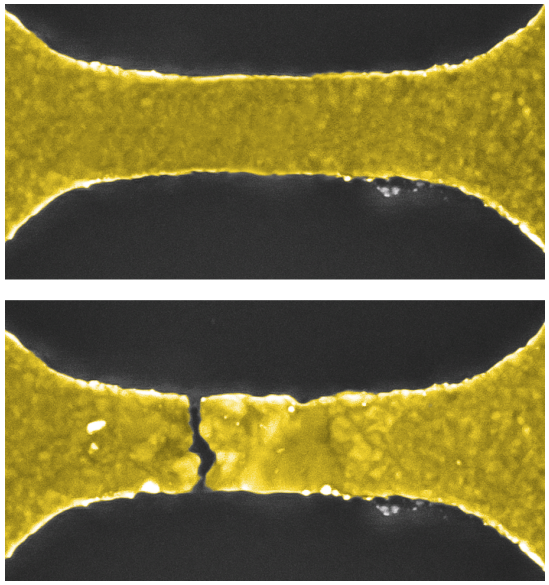

Figure 2.3: SEM image of gold (Au) bowtie: rendition before electromigration on top; after electromigration, with junction formed, on bottom (gold-colorized for emphasis).

transferring their momentum to local ions, resulting in ion movement [42, 43]. The electromigration process scales with current density so, as the structure narrows, the current density increases, causing the electromigration rate to increase. In other words, the electromigration process is a positive feedback system whose runaway end point would easily be a broken, open-circuit bowtie.

In addition to measuring specific junction configurations as mentioned above, electromigrated junctions have a number of other advantages:

- These lithographically created junctions are straightforward to use in many pre-

existing cryogenic dewer systems, due to the lack of mechanical parts. This is not

Figure 2.4: Shows two 3-axis piezo probes used to probe lithographically created devices at the bottom of an insertion stack [11].

often practicable with MCBJs or STM–BJs, which require mechanical feedthroughs, additional wiring, or components from outside of the cryogenic system.

- They are manufactured as a single component on a solid substrate, so the junction is virtually immune to vibrations.
- The silicon backplane, upon which the junction is created, makes the junction easy to gate.
- They are easy to incorporate with pre-existing high magnetic field systems. Leveraging pre-existing systems is important as the design and operation of these low-temperature, high-magnetic-field systems require special attention and specialized knowledge.

Electromigrated junctions also have some deficiencies:

- The junction can be incrementally broken with electromigration, but cannot be re-formed, as with the MCBJ (Section 2.1.1) or STM–BJ (Section 2.1.2).
- Not being able to re-form a junction also means more sample preparation, with additional time-consuming lithography.
- The RF shielding of all investigated dewer systems is not conductively watertight, resulting in signal quality degradation by EMI, Section 2.2.3.

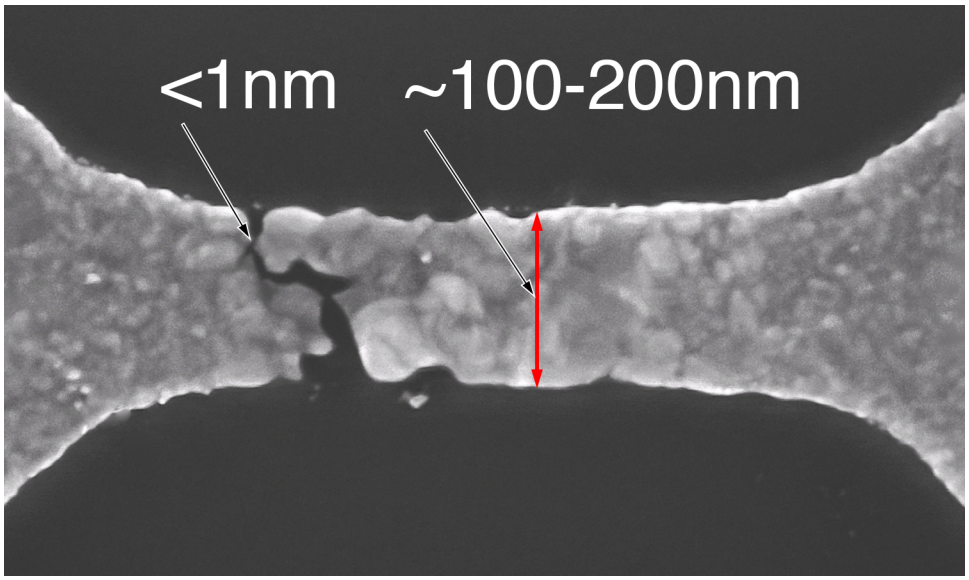

Figure 2.5: Shows an electromigrated Au bowtie break junction with typical dimensions.

The combination of the bowtie's mechanically static nature and low operating temperature makes for a considerably more stable junction than either the inchworm actuator MCBJ or the STM–BJ design. This stability allows for individual atomic configurations to be explored in detail rather than looking at ensemble averages, allowing for IV sweeps to be performed on single configurations.

Constructing these electromigrated bowtie junctions is time-consuming yet straightforward. The Au bowtie structures are patterned on top of an oxidized Si wafer using electron

beam lithography. On both sides of the 100–200 nm-wide constriction, the structure flares out to larger pads, where contact with our electrical probes is made. After lithography and development, 1 nm titanium (Ti) and 15 nm Au are evaporated onto the sample, followed by liftoff with acetone. The devices are cleaned by oxygen plasma for one minute immediately prior to being placed into the sample insert of a cryostat with four independently positionable probes (manufactured by attocube systems AG). This sample space is evacuated at room temperature and backfilled with 10 mb of helium (He) exchange gas. Once the sample is cooled to the liquid nitrogen temperature of 77 K, individual probes are put into electrical contact with the bowtie pads. Initial resistance of contacts, leads, and the device is 100–200 Ω. Once probed, electromigration is used to form the junction with typical structure sizes noted in Figure 2.5. Once the junction is formed, measurements can proceed, as covered in the next Section 2.2.

2.1.4 Comparison of Junction Formation Approaches

Figure 2.6 is a chart comparing the overall advantages and disadvantages of the various junction-forming approaches used in this research.

	MCBJ	STM–BJ	Electromigrated Junction
Fabrication Ease and Successful Sample Preparation/Use	Low	High	Medium
Operating Temperature	Room Temperature	Room Temperature	< 77K
Ability to Sweep Temperature	No	No	Yes
Configuration Stability	Milliseconds	Milliseconds	Hours
Data Type Provided	Averaging of Configuration Ensemble	Averaging of Configuration Ensemble	Single Configuration
Data Acquisition Productivity	Medium	High	Low
Physical Vibration Immunity	Medium	Low	High
EMI Immunity	Medium	High	Low

Figure 2.6: Comparison chart of MCBJ, STM–BJ, and electromigrated junction formation approaches.

2.2 Novel Measurement Electronics

The following sections will cover the electronic design used to measure the high-frequency shot noise and the conductance of the devices under test. The electronic design is highly leveraged among the inchworm actuator MCBJ (Figure 2.1), STM–BJ (Figure 2.2), and electromigrated junction (Figure 2.3) designs.

Although the input frequencies, time constants, and inconsequential wiring used among these experiments may differ slightly, electronic measuring circuits and associated test equipment are overwhelmingly the same. The differences in the electrical design used with the three test devices are trivial and will not be covered in this section.

At a high level, the measurement circuits and associated equipment are simultaneously measuring two characteristics: the conductance of the junction and its non-equilibrium

noise characteristics. The conductance of the junction is measured at low frequencies ($<$20 kHz) while the noise characteristics of the junction are determined at high frequencies ($\sim$200–700 MHz). Each measurement type and the associated portion of the measurement circuitry will be explained and diagrammed separately. Fortunately, it is possible to consider the low-frequency circuit and high-frequency portion of the circuit independently, because the disparate frequency signals are electronically isolated by passive bias tee RF components, as seen in Figure 2.10–G_1, G_2.

2.2.1 Low-Frequency Circuitry for Conductance Measurements

An offset square wave, sourced from a function generator, with a typical fundamental frequency of 2–15 kHz, toggles a voltage between $V_{min} = 0V$ and $V_{max} = V_{DC}$ across the junction (Figure 2.7–J). This low-frequency signal is used as a "DC" signal to measure conductance and to create the non-equilibrium conditions for simultaneous noise measurement described later. The signal proceeds from the junction through a current limiting resistance standard General Radio 1433-G Decade Resistor (Figure 2.7–H), and then to a Keithley 428-PROG current pre-amplifier (Figure 2.7–I). The resistance standard is used to avoid overloading the current amplifier input stage when the junction is in a fully shorted, high-conductance configuration. The output of the current amplifier is measured using a lock-in amplifier (Figure 2.7–D_2), Stanford Research SR830, synchronized with the input square wave, with a typical lock-in output time constant of $\sim$0.5–1 ms. The high-speed X and Y output of the lock-in is then digitized by a National Instruments data acquisition module (DAQ) 4084 (Figure 2.7–F).

The idealized circuit diagram can be seen in Figure 2.8, where V_T is known and applied by the function generator, i_T is known and measured by the pre-amplifier and the lock-in, R_{std} is set with the resistance standard, and R_{gen} is known.

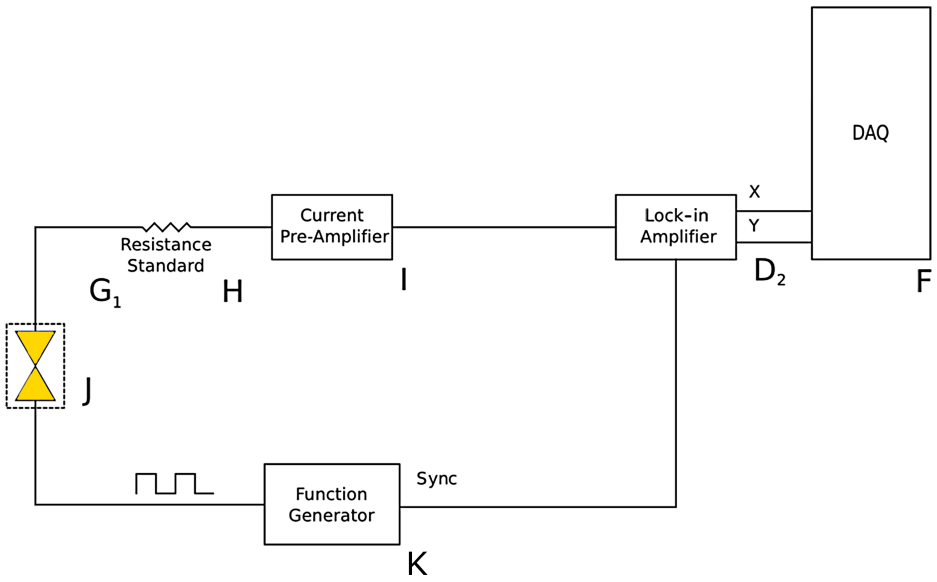

Figure 2.7: The low-frequency portion of the electronic design. The combined low-frequency and high-frequency circuit can be found in Figure 2.10. The total circuit with label explanation can be found in Appendix A.1.

The total circuit resistance, R_T, is determined by:

$$R_T = R_{gen} + R_{device} + R_{std} + R_{amp} = \frac{V_T}{i_T} \tag{2.2}$$

The resistance of the junction falls out as:

$$R_{device} = \frac{V_T}{i_T} - (R_{gen} + R_{std} + R_{amp}) \tag{2.3}$$

The conductance is merely the reciprocal of the resistance:

$$G_{device} = \frac{1}{R_{device}} \tag{2.4}$$

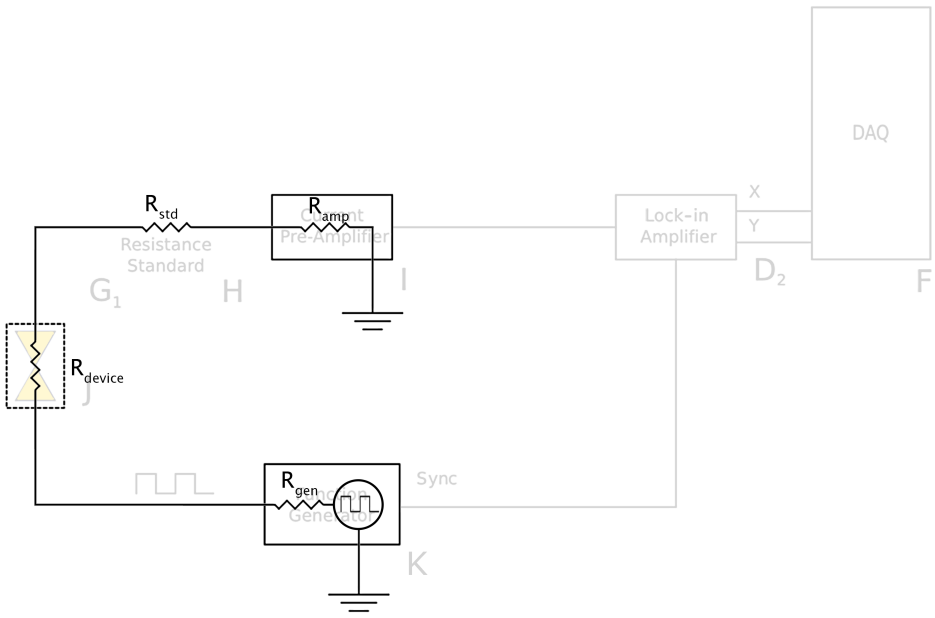

Figure 2.8: Where R_{gen} is the internal resistance of the function generator (Figure 2.7–K), R_{std} is the resistance of the resistance standard (Figure 2.7–H), R_{device} is the resistance of the junction (Figure 2.7–J), and R_{amp} is the internal resistance of the current pre-amplifier (Figure 2.7–I). See either Figure 2.7, the low-frequency diagram or Figure 2.10 for the full diagram (or Appendix A for the full diagram and annotation).

Armed with this information, it is possible to measure the conductance of the junction as it moves between connection and disconnection.

2.2.2 High-Frequency Circuitry for Shot Noise Measurements

2.2.2.1 Overview of High-Frequency Circuitry

The high-frequency portion of the measurement circuits and associated test equipment is used to determine the noise characteristics of the junction. With the application of a voltage difference across the junction (Figure 2.9–J), as performed in the low-frequency circuit description above, non-equilibrium noise, in addition to Johnson-Nyquist noise, is

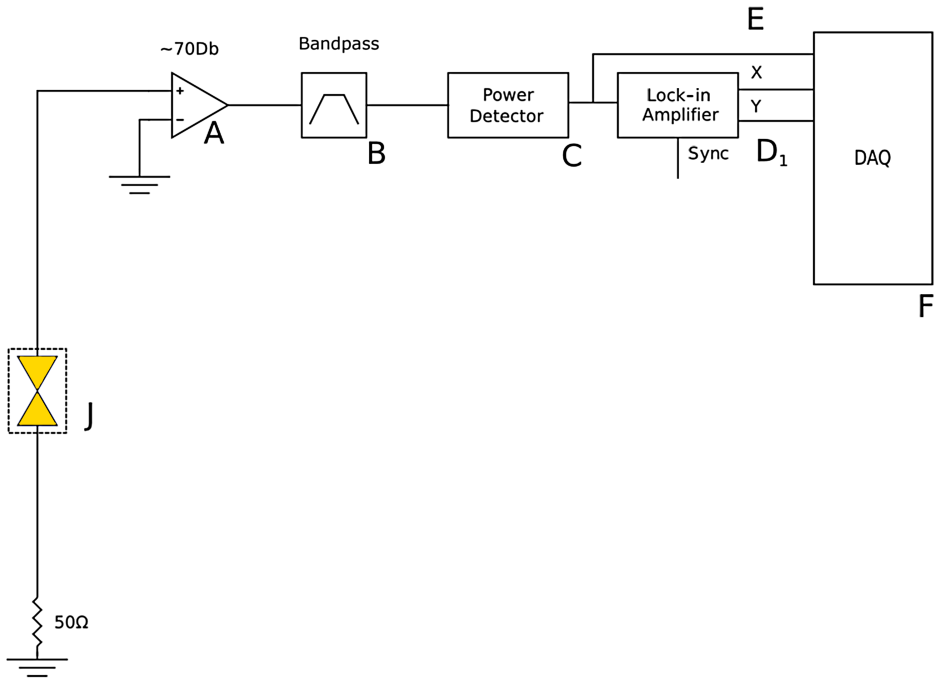

Figure 2.9: The high-frequency portion of the electronic design. The combined low-frequency and high-frequency circuit can be found in Figure 2.10. The total circuit with label explanations can be found in Appendix A.

generated in the device. A coaxial cable feeds this noise to a chain of amplifiers (Figure 2.9–A), with a nominal gain of $\sim$70 dB. The noise is then shaped/bandwidth–limited to $\sim$250–520 MHz, by a bandpass filter (Figure 2.9–B). This shaped power spectrum is passed to a logarithmic power detector (Figure 2.9–C), whose output feeds directly to the DAQ (Figure 2.9–F) through wire E (Figure 2.9–E), and also to a lock-in amplifier (Figure 2.9–D_1). The output of the lock-in amplifier (Figure 2.9–D_1) feeds directly to the DAQ (Figure 2.9–F).

The bandpass filter is used to limit the lower frequencies, which have more $1/f$ noise, to ensure a known repeatable measurement and workable signal-to-noise ratio. The power detector outputs a single voltage value that represents the integrated power over the bandwidth supplied by the bandpass filter. Translation of the voltage from the logarithmic power

detector to the input power to the detector is enabled by the output V = voltage versus input power graph (Figure 2.11) provided in the data sheet [44].

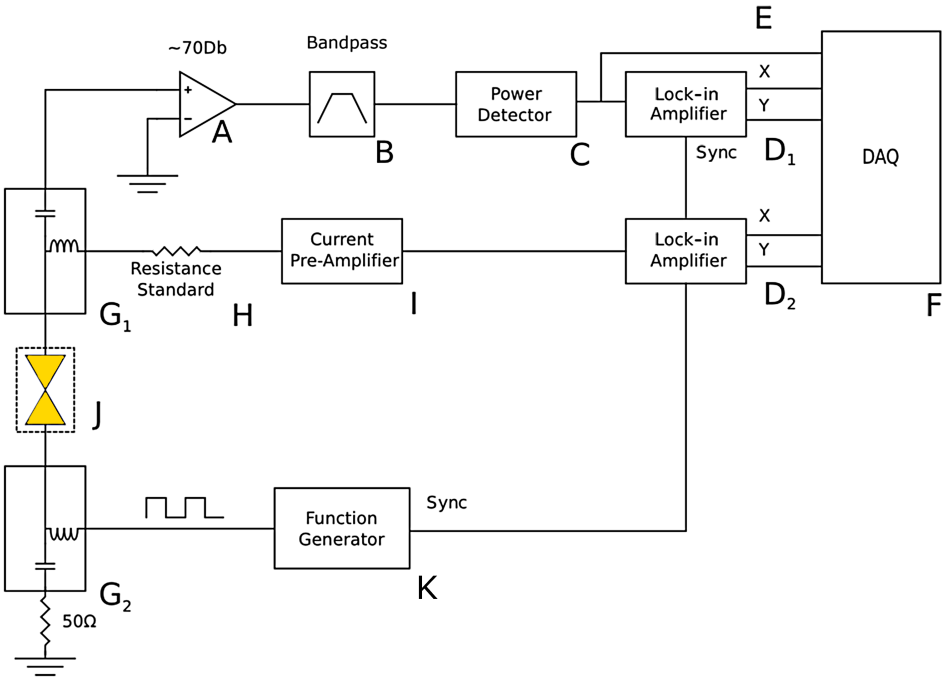

Figure 2.10: The complete electronic circuitry for the MCBJ, STM–BJ, and electromigrated junction experimental designs with both high and low-frequency portions of the circuit. The low-frequency portion of the circuit can be found in Figure 2.7, and the high-frequency portion in Figure 2.9. A full description of the diagram and components can be found in Appendix A.

2.2.2.2 Square-Wave Biasing of Junction

An offset square wave is used as the driving signal to the junction in this research, unlike many similar experimental designs using a lock-in (Figure 2.9–D_1). Shot noise power data extraction is straightforward, using a square wave that only applies two biases to the junction, since the magnitude of the shot noise is directly related to the bias voltage. Using a sine wave as the driving signal to a device makes shot noise data extraction more

complex, as its bias voltage varies over the entire waveform cycle. Substantially more data measurements would need to be taken over a wide sweep of DC offset values, followed by an integration process. A more detailed explanation follows:

- Since shot noise is a non-equilibrium noise, having 0 volts for half of the square wave cycle—in equilibrium conditions—makes certain no shot noise is generated during that half of the cycle. This ensures that the lock-in measurement does not filter out some shot noise as background noise.

- Junctions are inherently unstable, with relatively rapid change in atomic configuration, so quickly and accurately measuring junction characteristics at a given voltage is important. With the junctions tested in an MCBJ or STM–BJ system, measurements are averaged over tens of thousands of junction configurations, providing an ensemble result. As mentioned above, the sine wave approach would require integrating more measurements over a range of DC offset values to provide a shot noise power number with little numeric error.

- For measuring electromigrated junctions, the issues are similar. While electromigrated junctions at 77 K are more stable, the square-wave approach is still advantageous due to junction instability and additional background noise in the attocube, as covered in Section 2.2.3.

- Nonlinearity in the junction characteristics is seen at higher-bias voltages (Section 4.2). Since it is not necessary to integrate intermediate bias-offset voltage measurements with a square-wave approach, higher-bias voltages are more easily characterized. The voltage bias from a square wave immediately and directly allows measurement of the junction characteristics in any voltage region, including its nonlinear region,

while the measurements from a direct sine wave approach would mask the nonlinear characteristics.

2.2.2.3 Determining Absolute Power with Logarithmic Power Inputs to the Lock-In

The lock-in amplifier (Figure 2.9–D_1) is a great tool for filtering out unwanted signals whose peak-to-peak voltage could be many orders of magnitude larger than the signal of interest buried within the larger signal. Using a square wave as the driving signal to the junction (Section 2.2.2.2), the measured signal at the output of the lock-in is simply the non-equilibrium noise differential between 0 volts and V_{max} of the square-wave signal cycle.

Because the lock-in only measures this differential and the input to the lock-in is the logarithmic signal of the power detector, it is not possible to directly infer an absolute power measurement from the output signal of the lock-in. This is similar to a Δ value between two points on a logarithmic scale. Although that Δ has a fixed spacing between the points on that logarithmic scale, the absolute value of that Δ depends on its position on the logarithmic scale. Without additional information, the lock-in output signal could represent any amount of power.

To properly interpret the lock-in output signal as an absolute power requires measuring the output of the power detector directly through wire E (Figure 2.9–E) that goes from the power detector to the DAQ (Figure 2.9–F). The input from wire E, combined with the differential signal from the lock-in, allows the power output at both limits of the square-wave signal to be pinpointed and used to calculate an absolute power for the shot noise, as given by Equation (2.5):

$$P_T = PowerDetector^{-1}(PD_{avg} - \frac{V_{lockin}}{2}) - PowerDetector^{-1}(PD_{avg} + \frac{V_{lockin}}{2}) \quad (2.5)$$

where P_T is the power into the power detector due to the driving square wave, $PowerDetector$ is a function that converts the input power entering the power detector to the output voltage from the power detector, and $PowerDetector^{-1}$ is the inverse function which, when given the output voltage of the power detector, provides the power input required to create that output voltage. PD_{avg} is the mean output of the power detector over a time window, and V_{lockin} is the Δ difference input to the lock-in.

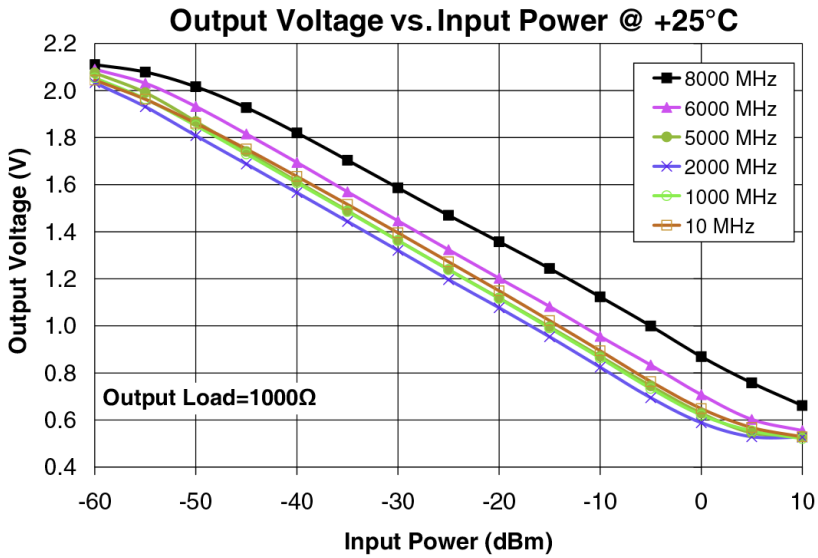

Figure 2.11: Shows the power detector's logarithmic scale/calibration curve, the input power [dBm] on the X axis, and the corresponding output voltage [V] on the Y axis for Mini-Circuits ZX47-60+ power detector. The $PowerDetector^{-1}$ function's transfer curve used in Equation (2.5) is derived from this graph.

2.2.3 Electromagnetic Interference Mitigation

Systems involving high-frequency components and small signal levels require careful attention to the electromagnetic shielding used in the experimental designs to avoid introducing noise into the measurement signal. At the beginning of this research, measurements included significant periodic and aperiodic RF noise from external sources and the lab test equipment. Low-frequency electronic equipment, such as the Stanford Research function generator DS345, the Stanford Research pre-amplifier, DC power supplies (such as those used to power the RF amplifiers), etc., were not designed to limit the amount of RF noise generated below the levels necessary to enable the shot noise signal measurements required by this research. If this background noise were just constant buzz, it would be filtered out by the lock-in and would not affect the measurements; however, external noise sources were not a constant background noise but, instead, changed regularly. Additionally, the environmental RF noise generated from the lab equipment often depended on subtle factors, such as placement and settings of neighboring instruments and even where the operator happened to be standing, impacting the resolution of the noise measurement and, in some extreme cases, requiring a recalibration of the shot noise measurement.

Trying to pursue a consistent background noise for lock-in filtering is a fool's errand. Determining the root cause of the shifting noise patterns, whether from lab instruments or external noise sources, was unfeasible. This dictated that providing good RF shielding would go a long way to ensure reproducible measurements in this experimental design.

One shielding approach is to use an electrically conductive enclosure known as a Faraday cage. The standard rule of thumb for the Faraday cage indicates that adequate shielding only requires a conductive mesh where the mesh spacing is $< 1/10$ the wavelength of the frequency of concern. Rules of thumb, by definition, are approximate and inexact. Some

use $1/5$ or $1/20$ instead of the $1/10$ rule. In this research, the maximum interfering-signal frequency of interest is $\sim$1 GHz. Applying the base Faraday cage rule of thumb indicates the spacing would have to be no larger than:

$$Spacing < 3x10^{8}[meters]/1GHz/10 = 3cm \tag{2.6}$$

which would allow gaps somewhat over an inch in size. All rules have their limits and so does the Faraday cage rule of thumb. In fact, this rule of thumb does not work for the extremely small signal measurements of this research, and conductive watertight boxes were required instead.

The inchworm actuator MCBJ (Figure 2.1) and the STM–BJ (Figure 2.2) feature a watertight conductive shielding around the junction being measured. In the MCBJ and STM–BJ, a large metal box is used to shield the sample from external RF noise. In addition, all low-frequency ports entering the RF tight container have low-pass filters that block any stray RF noise. The need to pay very close attention to all wires and connectors also became clear early on in this research. The difference between using a banana connection and a BNC connection (or, even better, an SMA connection; see Appendix C) to bias the junction was the difference between being unable to measure anything—because of environmental background noise—and the ability to measure a signal.

Using watertight conductive shielding and high-quality RF connectors yielded a measurement test environment where external noise sources were reduced in magnitude below the small shot noise signal levels of this research.

The attocube and associated cryogenic dewer system, however, have an EMI disadvantage. This is due to the lack of adequate RF shielding. Most commercial dewer systems are designed with some RF shielding, but since most industrial measurements have some

RF power pumped into the system, the shielding requirements are not as rigorous as those demanded by this research.

Chapter 3

Calibration and Proof of Concept

Because the measurement of shot noise suppression at room temperature had not previously been reported, it was crucial to validate our experimental design's model and assumptions with thorough, well-founded, and easily understood documentation to ensure the results would be accepted by the physics community. This chapter lays out the approach used to validate our experimental design:

- Ensuring proper calibration of losses in passive RF components and gains in active components.
- Showing that our technique is born from solid circuit analysis and ensuring it is well documented.
- Using a vacuum photodiode, as seen with measurement circuitry in Figure 3.1, with well-known noise characteristics as a reference for the MCBJ, STM–BJ, or electromigrated junction, and verifying that reference measurements of the shot noise follows the well known:

$$S_I = 2e\langle I \rangle. \tag{3.1}$$

After fleshing out the validation and calibration of the experimental design, this chapter will show how the same approach can be applied to MCBJ, STM–BJ, and electromigrated junctions.

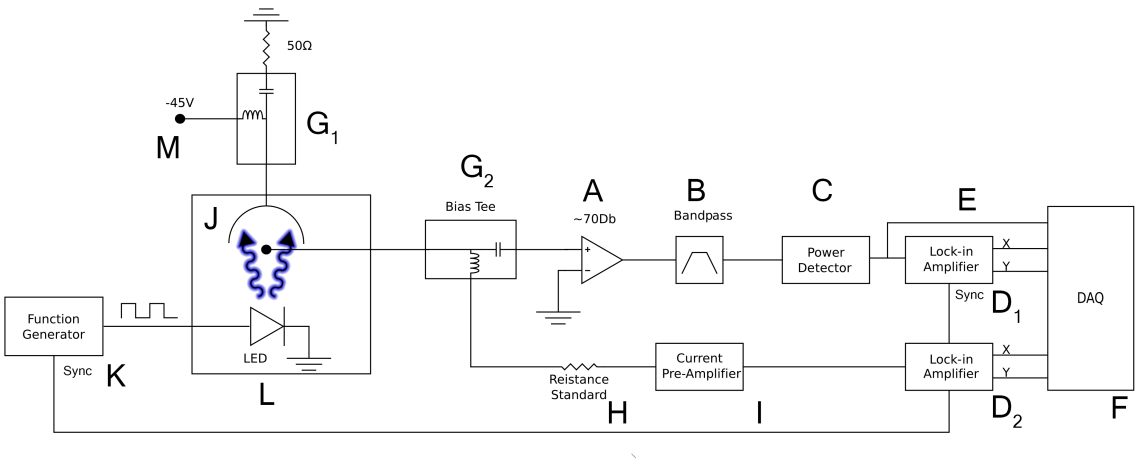

Figure 3.1: This diagram shows the high-frequency and low-frequency portions of the vacuum photodiode experimental design. A full description of the diagram and components can be found in Appendix B.

3.1 Existing Methods

The de facto standard impedance for most RF equipment is 50 Ω cables, 50 Ω terminated amplifiers, and so forth. Most industry equipment is matched to 50 Ω for maximum power transfer. Equipment that does not match this 50 Ω standard receives reduced power transfer because of reflections. In Figure 3.5, we see that the power transfer is greatly reduced, by at least eighty percent. A common strategy to avoid this loss in high-frequency circuits is to use a "tank" circuit [6]. This ensures a matching impedance over a limited bandwidth and minimizes loss due to reflection. The primary disadvantage of this tank-circuit approach is that the impedance matching only works over a narrow bandwidth and, as a side effect, attenuates the shot noise signal outside the bandwidth far below what would have been otherwise available.

The alternative approach used in our experimental design is to integrate the shot noise signal over a full 300–600 MHz spectrum, taking advantage of shot noise's broadband

white noise characteristics. Although the signal loss, because of the impedance mismatch and signal reflection, can be large, integrating measurements over hundreds of MHz of bandwidth gives as much as a 10^8 improvement factor relative to the narrow-band approaches. In other words, this experimental design allows the bandwidth to act as a signal multiplier.

3.2 Simplified RF Equivalent Circuit of Vacuum Photodiode

As shown in Figure 3.2-(a), the vacuum photodiode can be considered an ideal current source of mean square current fluctuations i_s^2 in parallel with a frequency-dependent impedance Z_s. The actual noise source is a two-port device at RF, terminated at one end by $Z_0 = 50\ \Omega$. The equivalent circuit parameters for the resulting single-port "generator" are then:

$$i_g = i_s \frac{Z_s}{Z_s + Z_0}, \tag{3.2}$$

$$Z_g = Z_s + Z_0 \tag{3.3}$$

In our experimental design, this generator is connected to a transmission line (characteristic impedance Z_0) and the RF amplifier chain (also Z_0). The current delivered to the Z_0 load is $i_0 = i_g Z_g/(Z_g + Z_0)$, and the power transferred to the Z_0 load is then:

$$|i_0|^2 Z_0 = Z_0 i_s^2 |\frac{Z_s}{2Z_0 + Z_s}|^2. \tag{3.4}$$

If one considered a reflectance measurement looking from a 50 Ω line into the generator,

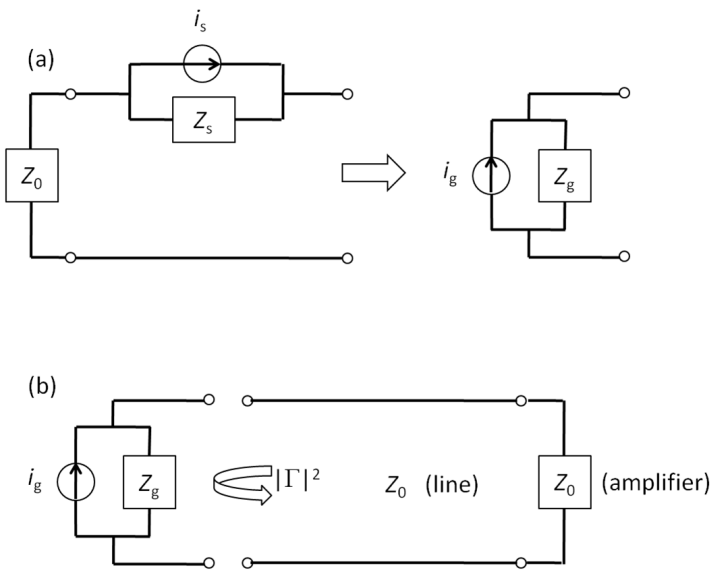

Figure 3.2: (a) Equivalent circuits for noise current sources. The sample itself has some short-circuit RMS current noise, i_s, and effective impedance, Z_s. Terminating one end of the sample with Z_0 results in a single-port equivalent circuit with RMS current noise i_g and impedance Z_g, as explained in Section 3.2. (b) Schematic of the reflection measurement relevant to determining the actual power transferred from the sample to the amplifier chain.

Figure 3.2-(b), one would find:

$$\Gamma = \frac{Z_g - Z_0}{Z_g + Z_0} = \frac{Z_s}{2Z_0 + Z_s}. \tag{3.5}$$

Thus, the power transferred to the Z_0 load is $i_s^2 Z_0 |\Gamma|^2$, in the limit that $Z_s >> Z_0$, $\Gamma \to 1$.

3.3 Characteristic Impedance of Vacuum Photodiode

Figure 3.3 shows the circuit configurations used to measure the reflection coefficient of the terminated vacuum photodiode.

Figure 3.4 shows the circuit configurations used to measure the gain-bandwidth product of the nominally 50 Ω amplifier chain. Gain was measured by comparing output power

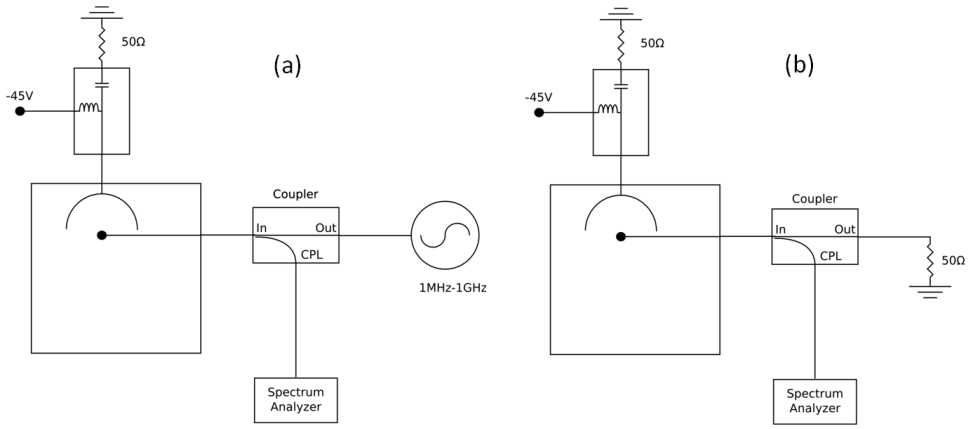

Figure 3.3: Schematics of circuits used to measure the RF reflection coefficient of the vacuum photodiode over the bandwidth of interest. The directional coupler has a coupling factor of -20 dB. The left circuit measures the reflected power at fixed frequency, and the spectrum analyzer's RF source is swept over 1000 discrete frequencies, ensuring all relevant features are captured. The right circuit measures the background noise power of the system.

referenced with a known input power for more than 1000 discrete frequencies across the bandwidth of interest, ensuring all relevant features are captured.

Figure 3.5-(a) is the measured gain as a function of frequency for the amplifier chain and filters. Figure 3.5-(b) shows the measured fraction of reflected power, $|\Gamma|^2$, for the vacuum photodiode over the same frequency range, obtained with the approach in Figure 3.4. Figure 3.5-(c) shows the convolution of the gain-bandwidth product and $|\Gamma|^2$. As shown in the previous section, this convolution may be used to infer the original mean square current fluctuations, i_s^2, from the photodiode noise source. The results of this procedure with the vacuum photodiode are shown in Figure 3.7.

Figure 3.6 shows DC current-voltage characteristics of the vacuum photodiode around its DC operating point (-45 V) for three of the illumination levels (labeled by the voltages applied to the illuminating LED) used in the photodiode shot noise measurements. The DC resistance is always much larger than 50 Ω, as explained in Section 3.5 and Figure 3.6.

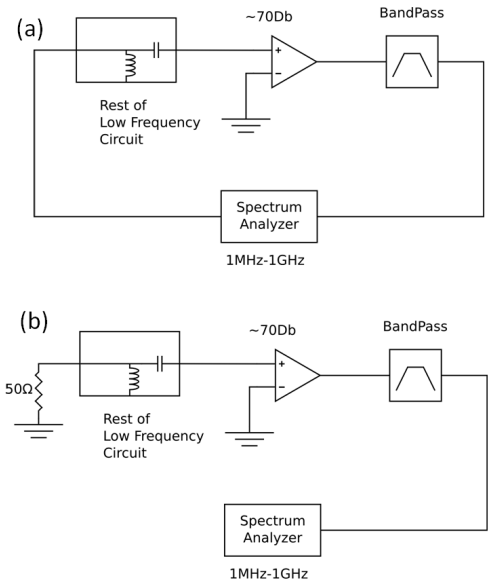

Figure 3.4: (a) Schematic diagram showing design for measuring the gain-bandwidth product of the amplifier chain used in the experiments. The rest of the low-frequency circuit branch includes the resistance standard, current amplifier, and lock-in amplifier shown in Figure 2.7 and in the complete circuit diagram in Appendix A. (b) Schematic diagram showing circuit for background noise measurement in gain-bandwidth product configuration.

What does matter is the RF response of the terminated vacuum photodiode. As the $|\Gamma|^2$ data show, the impedance mismatch over the bandwidth of interest is not nearly as severe as one would infer from purely DC measurements.

3.4 Calibration Methodology through Gain-Bandwidth Product

Conversion of the measured noise power into units of current noise per unit bandwidth requires knowledge of $|\Gamma|^2$ and the gain-bandwidth product, g, of the amplifier chain. An RF source is cycled through 1000 evenly spaced frequencies, f, from 1 MHz to 1 GHz, feeding an input power, $P_{\rm in}(f) = -80$ dBm, into the amplifier chain. The output of the amplifier chain, $P_{\rm fg}(f)$, is recorded at each frequency (with $P_{\rm in}(f) > 0$), as is the background

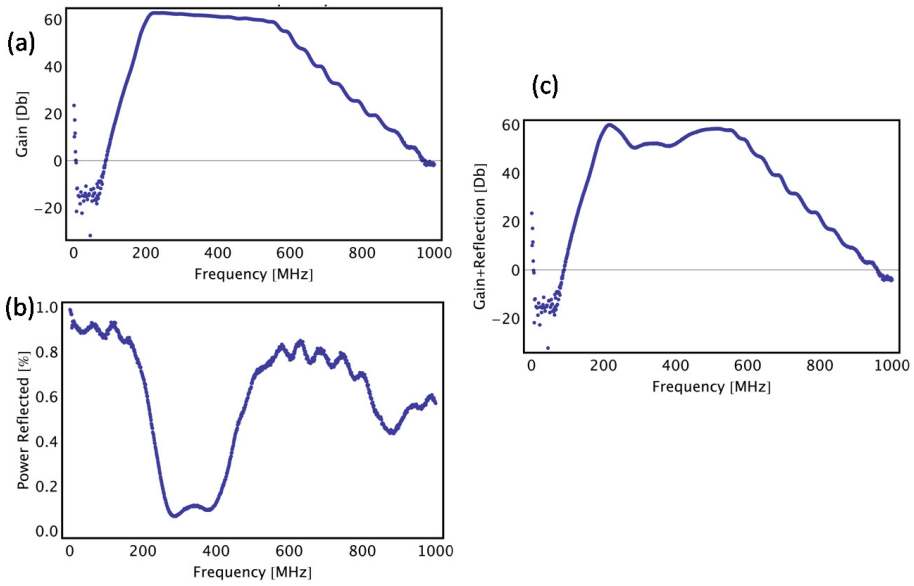

Figure 3.5: (a) Measured gain versus frequency obtained using the circuit in Figure 3.4. (b) Fraction of power reflected by the vacuum photodiode as a function of frequency, obtained using the circuit in Figure 3.3. (c) Convolution of the gain-bandwidth product and $|\Gamma(\omega)|^2$, used to infer the photodiode current noise from the measured RF power, as described in the Section "Characteristic Impedance of Vacuum Photodiode" 3.3.

output (with $P_{\text{in}}(f) = 0$). The gain-bandwidth product is then computed by numerical integration of the gain, as seen in Figure 3.5-(a):

$$g = \int \frac{P_{\text{fg}}(f) - P_{\text{bg}}(f)}{P_{\text{in}}(f)} df \tag{3.6}$$

A separate measurement of $|\Gamma(\omega)|^2$ of the photodiode at each frequency, as seen in Figure 3.5-(b), allows us to correct g for the division of power between the photodiode and the amplifier chain. The measured noise power is then divided by this corrected gain-bandwidth product to infer the power noise per Hz delivered to the amplifier chain. Finally, this is divided by the input impedance of the first stage amplifier, 50 Ω, to obtain the current noise per Hz produced by the photodiode.

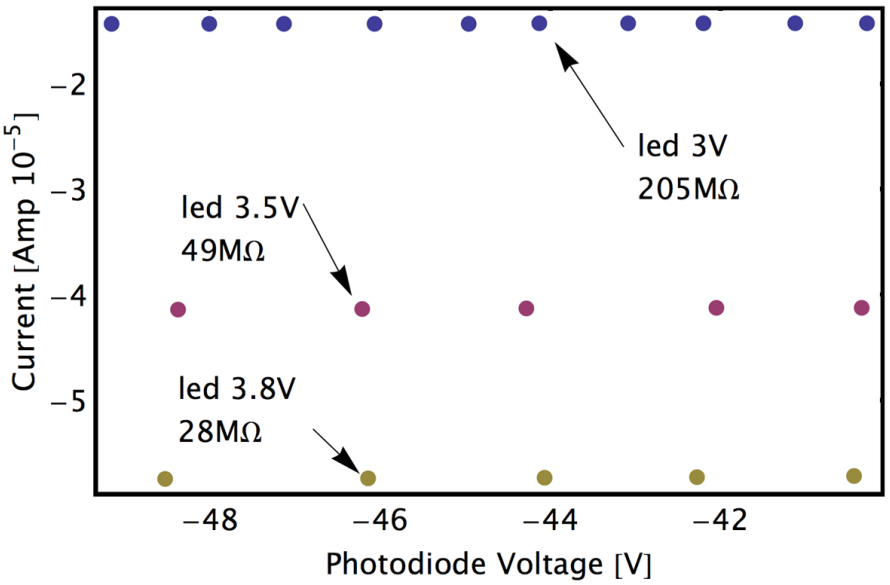

Figure 3.6: Current-voltage characteristics of the photodiode at three illumination levels (indicated by LED voltages) near the photodiode DC operating point of -45 V. Differential resistances at -45 V are indicated.

3.5 In Situ Measurements of Vacuum Photodiode – Proof of Concept

Vacuum photodiodes have well-known noise properties, making them ideal to characterize and calibrate the experimental design. As shown in Figure 3.6, the photodiode has a DC resistance several orders of magnitude larger than the 1–100 kΩ that is relevant in the MCBJ, STM–BJ, and electromigrated junctions.

As shown in Figure 3.7, this noise scales linearly with the photocurrent, resulting in a slope of $3.29 \pm 0.02 \times 10^{-19} A^2/Hz$. This compares well with expectations, deviating from the expected $2e$ by less than three percent. This shows that not only is our calibration correct, but that it is also possible to measure shot noise in devices that have a DC resistance 10 to 100 times the resistance of MCBJ, STM–BJ, or electromigrated junctions. Now that the experimental design has been validated, let us look at more interesting systems.

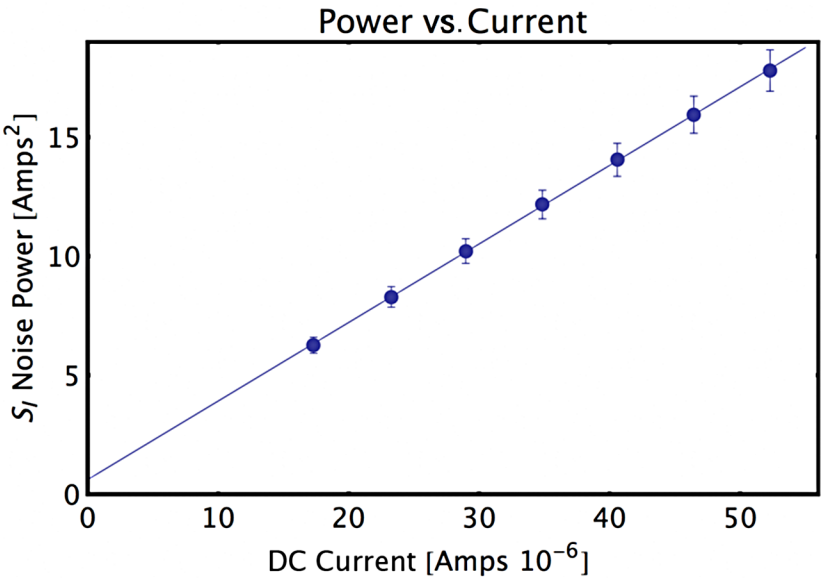

Figure 3.7: Shot noise [A^2/Hz] as a function of (square wave) current through the photodiode (tuned by various LED illumination intensities). The small offset indicates a small noise background and the slope is consistent with the expected $2eI$ to within three percent. This shows successful shot noise measurement for the photodiode and serves as a proof of concept for our measurement circuitry, calibration, and overall technique.

3.6 Characteristic Impedance of a Junction

Figure 3.8 shows the circuit configuration for reflectance measurements on the break junctions, the data for $|\Gamma|^2$ as a function of G for a single frequency, 300 MHz. Performing such measurements at many discrete frequencies across the full bandwidth is very tedious. The primary point to observe here is that $|\Gamma|^2$ is essentially independent of G when $G >\sim 0.5G_0$. The approximate invariance of the reflection versus G allows the excess noise to be calculated without having a real time, broadband measurement of the reflection. A likely explanation for this invariance is that the junction impedance is dominated by other geometric and experimental factors instead of the atomic-scale arrangement of the last couple of atoms. Most high-end spectrum analyzers do not offer the data acquisition rate and point density needed to take such a real-time measurement and would require cus-

tom hardware, so it is fortuitous that this is not necessary for our purposes. Now that the presented approach has been shown to be reasonable for the photodiode reference case and junctions, let's look at the results that it enables.

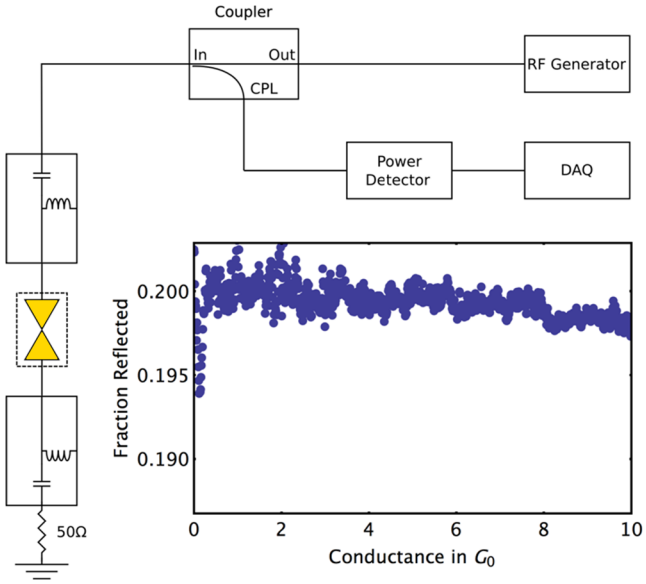

Figure 3.8: Schematic diagram for measuring the reflectance of the junction devices. Not shown are the rest of the low-frequency electronics hooked to the DC inputs of the bias tees, as in Figure 2.7, or in the full-circuit description in Appendix A. Inset graph: Reflectance versus G at 300 MHz.

Chapter 4

Experimental Results

This chapter has two major sections, with the first covering the results, analysis, and summary using the MCBJ setup at room temperature, followed by a section with the results, analysis, and summary using the electromigrated junction setup at the liquid nitrogen temperature of 77 K.

4.1 MCBJ Shot Noise Measurements at Room Temperature

4.1.1 Results and Analysis

Using the experimental design from Sections 2.1.1 and 2.1.2, conductance and noise data are recorded simultaneously as the junction is brought in and out of contact, as described in Section 1.5, using a National Instruments 4084 (Figure A.1–F), DAQ to sample the lock-in outputs at $\sim$1000 samples per second. Histograms of the measured conductance values are compiled in real time during junction breaking and formation, while running averages and standard deviations of the noise power are computed for each conductance bin. The data analysis is entirely automated, with no post-selection of "nice" traces. In general, conductance traces were cleaner, with more observable conductance quanta, during junction breaking rather than formation.

Figure 4.1 shows an example data set acquired at room temperature over several hours. The conductance histogram shows peaks at approximately 1, 2, and 3 G_0, as expected from previous work on Au junctions [37]. Deviations from perfect quantization at integer

multiples are seen in some samples, but are always quantitatively consistent with previous measurements on Au junctions at room temperature with work hardening [45]. The average

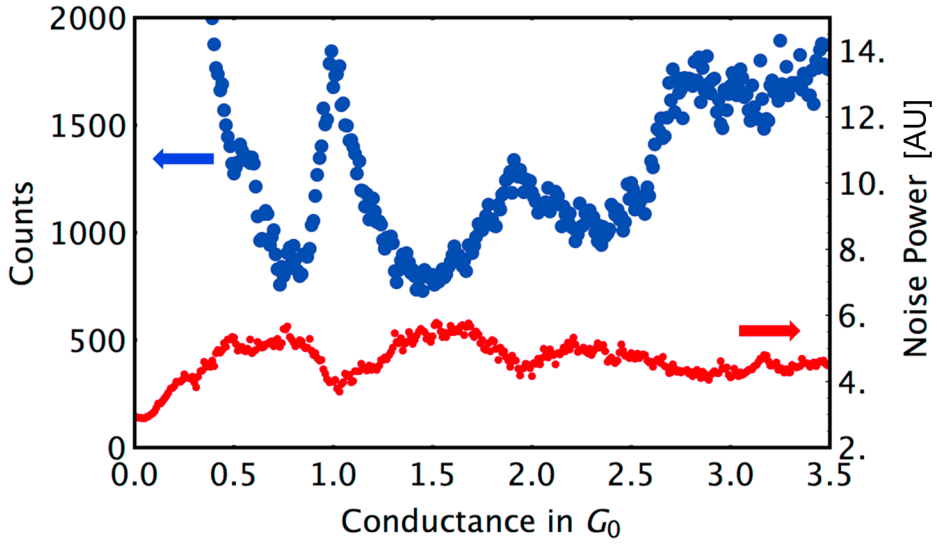

Figure 4.1: Simultaneously acquired conductance histogram (upper curve, left axis) and averaged shot noise (lower curve, right axis). These data were taken at room temperature with V_{DC} = 100 mV, and square-wave frequency $\sim$1 kHz.

noise power distribution shows significant dips in power centered close to the conductance values associated with peaks in the histogram. This noise suppression is very similar to that seen by van den Brom et al. at liquid He temperatures [8]. Note that the suppression is not expected to reach all the way to $F = 0$, as seen from Figure 1.11, because, statistically, junctions with $G = G_0$ may be formed in many ways, with many possible combinations of τ_i for various channels, and not just the first and only channel fully open.

As described by van den Brom and van Ruitenbeek [8], one can construct an explicit model of the expected shot noise by assuming a form for the contributions of various conductance channels as a function of conductance. This is likely to be reasonable only in the small number of channels limit. Figure 4.2 shows such a model, while Figure 4.3 plots the

corresponding expected shot noise, based on Equation (1.11), for various magnitudes of DC (square-wave) bias.

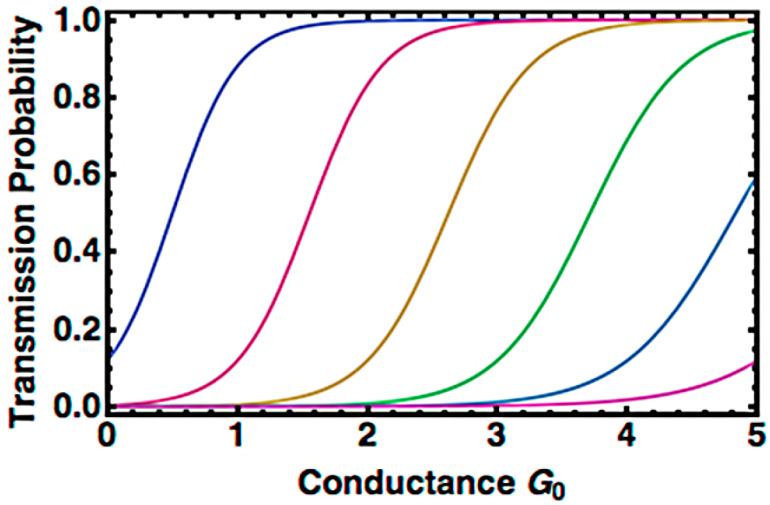

Figure 4.2: One choice of relevant transmission coefficients as a function of junction conductance. This is similar to the approach taken by van den Brom and van Ruitenbeek [8] (Figure 1.8).

The calculations assume a temperature of 300 K, and consider that the actual voltage dropped across the junction is $V = V_{\mathrm{DC}}(1/G)/(1/G + R_{\mathrm{ser}})$, where R_{ser} is the resistance standard, approximately 6 kΩ for the measurements in Figures 4.1 and 4.4.

Comparisons with high-bias data sets are of considerable interest because higher biases enable possible inelastic processes, such as optical phonon scattering, and there are theoretical predictions [46, 47] (particularly in molecular junctions [48, 49]) that such processes can modify the Fano factor away from the prediction of Equation (1.11) (repeated here for convenience).

$$S_I = 4k_{\mathrm{B}}TG_0 \sum_i \tau_i^2 + 2eV \coth \frac{eV}{2k_{\mathrm{B}}T} G_0 \sum_i \tau_i(1-\tau_i). \tag{4.1}$$

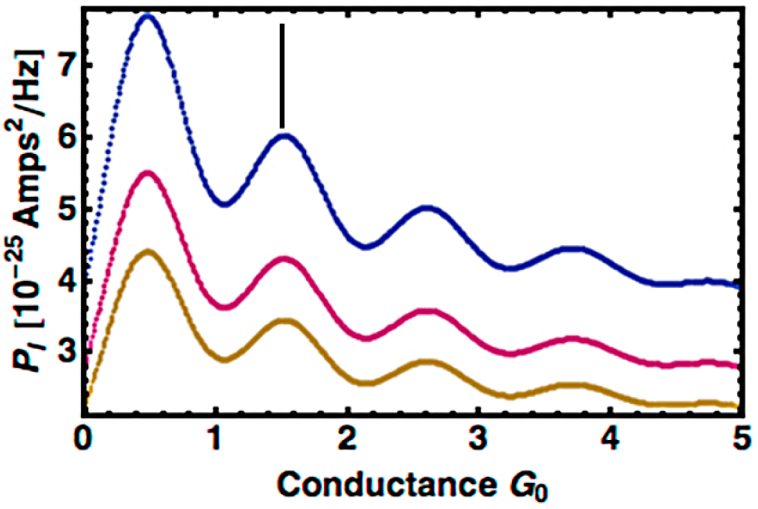

Figure 4.3: Predicted current noise with no Nyquist-Johnson component, for (bottom to top) $V_{\mathrm{DC}} = 80$ mV, 100 mV, and 140 mV, calculated from Equation (4.1) using the transmission coefficient distribution shown in Figure 4.2 and recalling that V across the junction varies with G because of the series resistor. The vertical line shows the equivalent change in current noise expected at that conductance for a temperature change of 20 K.

Magnetic processes can also lead to unconventional Fano factor values [50]. The calculations behind the results shown in Figure 4.3 assume no such modifications.

Figure 4.4 shows averaged measured noise power as a function of conductance for the same V_{DC} magnitudes as in the model of Figure 4.3. No background subtraction has been performed and, as above in Figure 4.1, no correction has been made to the noise data to account for the dependence of $|\Gamma(\omega)|^2$ of the junction on the conductance since, as shown in Figure 3.8, this reflectance is mostly invariant over the conductance of interest.

Comparison between the model and the data reveals several features of interest. The trend at high conductances toward lower noise with increasing G is expected because of the resistance standard: when $G >> R_{\mathrm{ser}}^{-1}$, the DC current approaches $V_{\mathrm{DC}}/R_{\mathrm{ser}}$, and the DC voltage, V, relevant for Equation (4.1), becomes small, because most of the applied DC

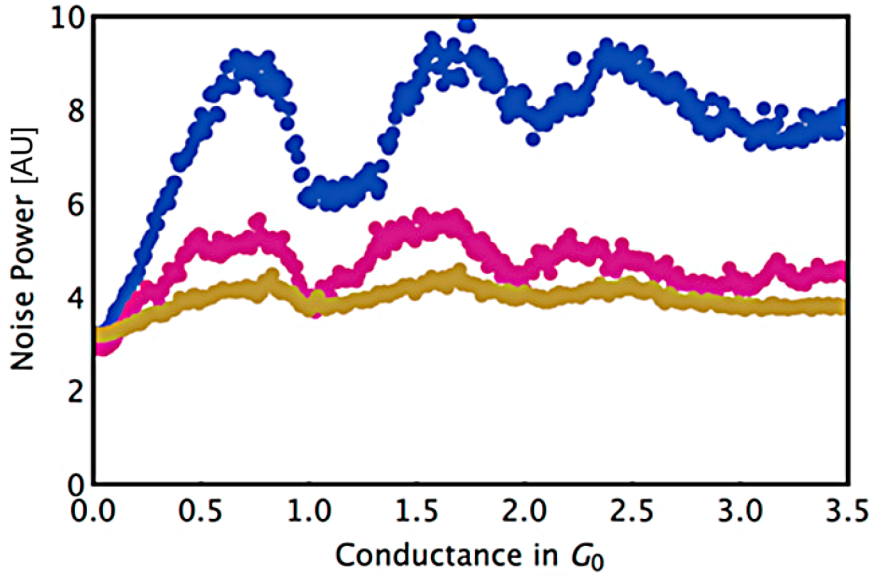

Figure 4.4: Measured noise power as a function of conductance for (bottom to top) $V_{\mathrm{DC}} = 80$ mV, 100 mV, and 140 mV on a particular break junction, with no background subtraction.

voltage is dropped across the resistance standard. The deviation of the data from the model at low conductances ($G <\sim 0.5G_0$) is not surprising, given the sensitivity of that data to the reflection coefficient resulting from the impedance mismatch between the junction and the amplifier chain.

One must be concerned about contributions to the data because of $1/f$ noise. In electronic conduction, this noise results from temporal fluctuations of the resistance with a broad distribution of characteristic timescales [1, 51]. This noise has been shown to exist in metal contacts approaching the atomic scale [21]. Static conductance fluctuations as a function of DC bias voltage across nanojunctions are suppressed near quantized conductance values [52]. It is conceivable that the time-dependent conductance fluctuations that cause $1/f$ noise could be similarly affected by the decreased backscattering and increased junction stability near quantized conductance values. To test for this physics, we

consider the dependence of the measured noise on the DC current through the junction. At a given G, conductance fluctuation noise is expected to be *quadratic* in the DC, in contrast with shot noise. We do not see strong signatures of such a dependence, as shown in Figure 4.5, finding that the measured noise is roughly linear in DC, extrapolating toward a finite background value at zero current. There is some nonlinearity, however, meaning that

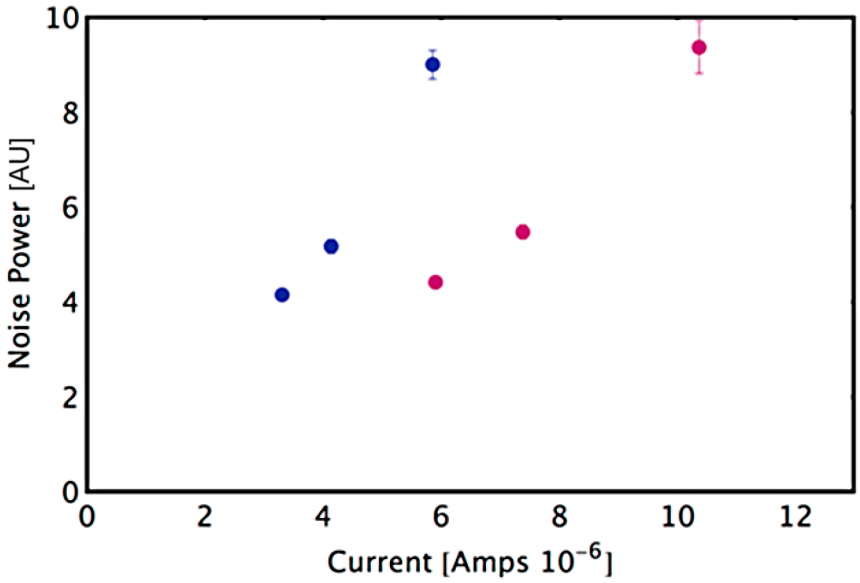

Figure 4.5: Measured noise power as a function of DC bias current at two conductances. Dependence on the DC is slightly superlinear. Possible explanations for this are discussed in the text.

some contribution from $1/f$ noise cannot be completely ruled out. Further work by Ruoyu Chen, in [41], leveraging the same experimental apparatus and design, has shown that, at conductances with strong shot noise suppression, the remaining excess noise fits well with a quadratic function, as would be expected by flicker noise theory, and compatible with flicker noise findings in [21].

4.1.2 MCBJ Summary

The presence of noise suppression at room temperature shows explicitly the quantum character of transport in these atomic-scale devices. Inelastic processes, such as electron-phonon scattering, can remove energy from the "hot" electron system and redistribute electrons among the various quantum channels. This is what leads to the suppression of shot noise in macroscopic conductors at room temperature. These data suggest that such inelastic processes operate on length scales longer than the single-nanometer junction size, even at 300 K and biases in the tens of mV range.

An additional contribution to the superlinearity seen in Figure 4.5 that must be considered is bias-driven local electronic heating of the junction. Such heating would be synchronous with the bias current, and thus would be detected in the lock-in technique. Bias-driven ionic heating has been inferred in such junctions previously by studying the bias dependence of the junction-breaking process [53]. It has also been noted that effective temperature changes in robust junctions can reach several hundred Kelvin at biases of a few hundred mV [54]. An effective increase in the electronic temperature (which is relevant to Equation (4.1)) would not have to be very large to be detectable. The plausibility of this explanation is reinforced by the vertical line shown in Figure 4.3, indicating the change in Johnson-Nyquist current noise expected for a 20 K electronic temperature change at that conductance.

Such electron heating has been considered theoretically in some detail [46, 47, 55]. In fact, the authors of the latter [55] explicitly suggest using measurements of the noise as a means of detecting local, non-equilibrium heating in atomic-scale contacts. Detailed modeling of the local junction temperature is complicated because the local Joule heating and effective thermal path are explicit and implicit functions, respectively, of G. Further work done by Ruoyu, in [56], with the same experimental apparatus, shows strong evidence

that this in-phase heating is in effect and can, in good part, be modeled by Equation (1.6), at least above $2G_0$ in conductance.

This technique raises the possibility of performing rapid assays of shot noise through molecules, given the great progress that has been made in recent molecular break junction conductance measurements. As mentioned above, both electron-vibrational effects and magnetic processes are predicted to modify Fano factors away from $F = 1$. However, small molecule conductances tend to be on the order of $10^{-5} - 10^{-2}\ G_0$. Such low conductance junctions have, necessarily, very poor impedance matching to the usual 50 Ω RF electronics used in the noise measurements. Moreover, there is great interest in examining noise in such systems at much lower bias currents. Improved coupling of junction noise power to the amplifiers and reduced backgrounds would be a necessity. Impedance-matching networks, or tank circuits, may provide a means of adapting this approach to the molecular regime, though not without a likely reduction in bandwidth.

We have used high-frequency methods to observe shot noise suppression in atomic-scale Au junctions at room temperature, which show clearly the quantum character of conduction in these nanodevices. High-frequency methods allow the rapid acquisition of noise data simultaneously with statistical information about conduction in ensembles of junctions. A slightly nonlinear dependence of the measured noise on DC bias current raises the possibility that local heating and $1/f$ noise may need to be considered in these structures. Although impedance matching for low conductance junctions is a challenge, the prospect of adapting this approach to study noise in molecular junctions is appealing.

4.2 Electromigrated Junction Shot Noise Measurements at 77 K

4.2.1 Results and Analysis

One limitation of the MCBJ design used above is that it averages over an ensemble of junction configurations. Anything of interest that happens only a minority of the time will be lost even when looking at the standard deviation and self-correlation. In order to gain insight into these individual configurations, we will turn to using electromigrated junctions at 77 K.

Using the experimental design from Section 2.1.3, data was gathered on electromigrated junctions while being tested at 77 K. Figures 4.6, 4.7, 4.8, and 4.9 show raw, averaged current noise as a function of DC current for a particular junction electromigrated to a DC resistance of approximately 3 kΩ, so the conduction is expected to proceed through a small number of quantum channels. Some nonlinearity is present in such a plot, and it is necessary to determine whether this originates from finite-temperature effects or other noise processes. When comparing the bias dependence of the noise with the simple finite temperature expectations of Equation (4.1), we follow the approach of Kumar et al. [12] by scaling the data for plotting purposes. The change in current noise due to the bias, $P_I \equiv S_I(V_{\rm DC}) - S_I(0)$, inferred from the lock-in measurements of the power detector, is normalized by the expected Johnson-Nyquist noise, $P_T \equiv 4k_BTG$, and plotted as a function of a scaled bias coordinate:

$$X(V_{\rm DC}) = \frac{eV}{2k_{\rm B}T}\coth\frac{eV}{2k_{\rm B}T} - 1 \tag{4.2}$$

In these scaled plots, normalized noise in accordance with Equation (4.1) should be linear in $X(V_{\rm DC})$, with a slope given by the zero temperature Fano factor and an intercept of zero at $X = 0$, with identical response for positive or negative polarity of $V_{\rm DC}$.

At least 86 junction configurations examined show simple, linear noise data consistent with these expectations (a number of additional junction configurations had insufficient data collection to guarantee reproducible, stable linear response at both polarities of bias). An example of this linear dependence is seen in Figure 4.6. Assuming that the calibration procedure described above is absolutely correct, the Fano factor for this device is approximately 0.036 [8]. The simplest way of reconciling this low Fano factor with the restriction of a small number of contributing channels is that the calibration procedure is not precise and that conduction in this particular junction is dominated by four nearly fully transmitting channels, as typically found in monovalent metals [8]. The important point for this and similar junction configurations is that the bias dependence of the noise is functionally identical to the expectations of Equation (4.1), assuming a constant Fano factor over the applied bias range.

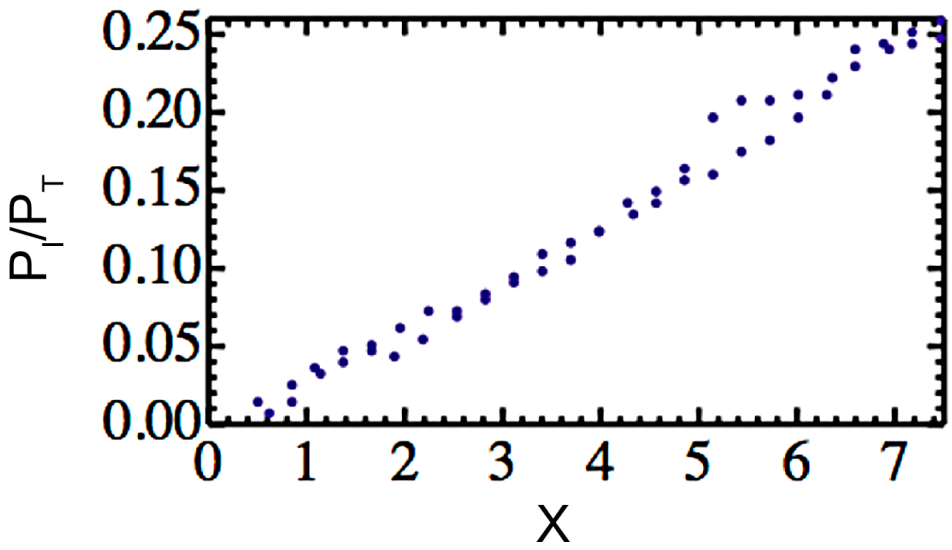

Figure 4.6: A scaled plot of normalized excess noise as a function of scaled bias for the junction in Figure 4.11. The linearity of this plot shows that the nonlinearity of around 0 volts in Figure 4.7 originates from the expected functional form of finite-temperature shot noise, as in Equation (4.1).

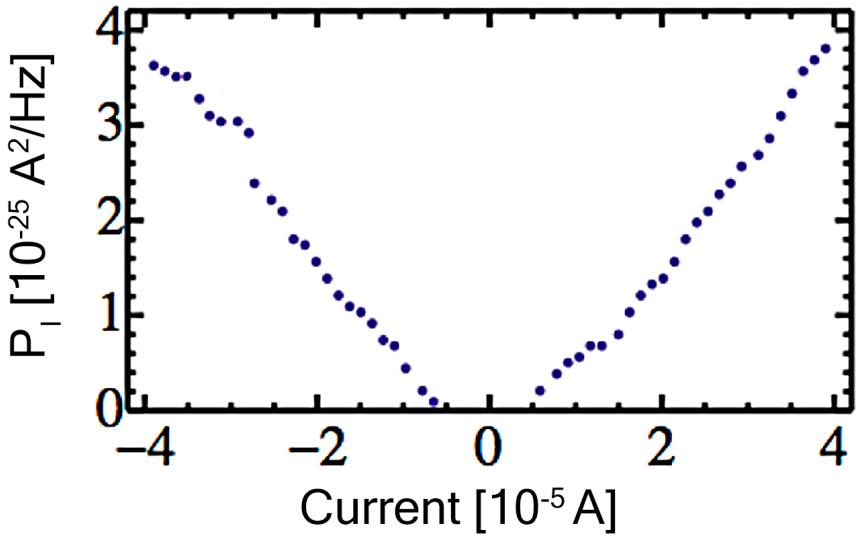

Figure 4.7: Inferred excess noise as a function of current in a junction with zero-bias resistance of 3 kΩ, showing intrinsic nonlinearity around 0 volts.

In contrast, some devices show clear deviations from expected linear dependence of P_I/P_T on X, suggesting either a voltage-dependent Fano factor or noise processes not encompassed by Equation (4.1). Examples of such deviation are kinks in the noise as a function of bias when V_{DC} is in the tens of millivolts range, as seen in Figures 4.8 and 4.9. Assuming that the noise is the excess noise of Equation (4.1), the sudden change of slope at a particular bias indicates a change in Fano factor. Similar changes in slope have been observed in twenty junction configurations, sometimes with slopes increasing above a critical voltage (Figure 4.9) sometimes with slopes decreasing above a critical voltage (Figure 4.8). In such junctions, these kinks are repeatable and stable over many bias sweeps. In terms of voltage across the junction, these kinks appear at an average of 52 mV bias, with a standard deviation of 14 mV. This bias level is approximately an order of magnitude below the bias range where electromigration is normally observed. We note that there is no obvious corresponding nonlinearity observed in the current-voltage charac-

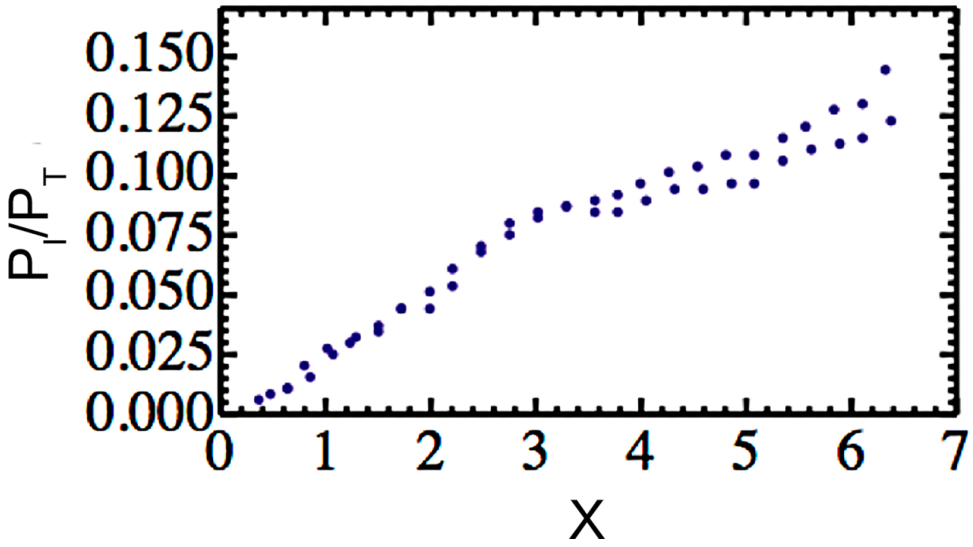

Figure 4.8: Examples of discrete changes in Fano factor at particular threshold voltage biases of tens of mV. Such changes in slope are consistent with previously reported observations [12] of inelastic electronic interactions with local vibrational modes, though in this case the junctions involve many conductance channels. The junction in this figure has a resistance of $600\ \Omega$.

teristics, though the measurement technique used here (measuring I directly at each value of V_{DC}) precludes easy simultaneous measurement of the higher derivatives of I versus V_{DC}, traditionally performed using lock-in methods. The sensitivity of device properties to atomic-scale details of junction configurations has made it very difficult to change back and forth between the standard lock-in approach for measuring dI/dV and d^2I/dV^2 and the noise measurement approach without affecting the junction. Attempts to improve the situation are ongoing. Recent additions of the metal flange and feedthroughs may go a long way toward making this possible. Voltage-thresholded changes in the excess noise have been described in a large number of models that describe electronic transport with a small number of transmitting channels in the presence of electronic coupling to a local vibrational mode [47, 48, 57, 58, 59, 60]. For example, recently, Kumar et al. observed qualitatively similar kinks close to $G = 1G_0$ in atomic-scale Au junctions (dominated by

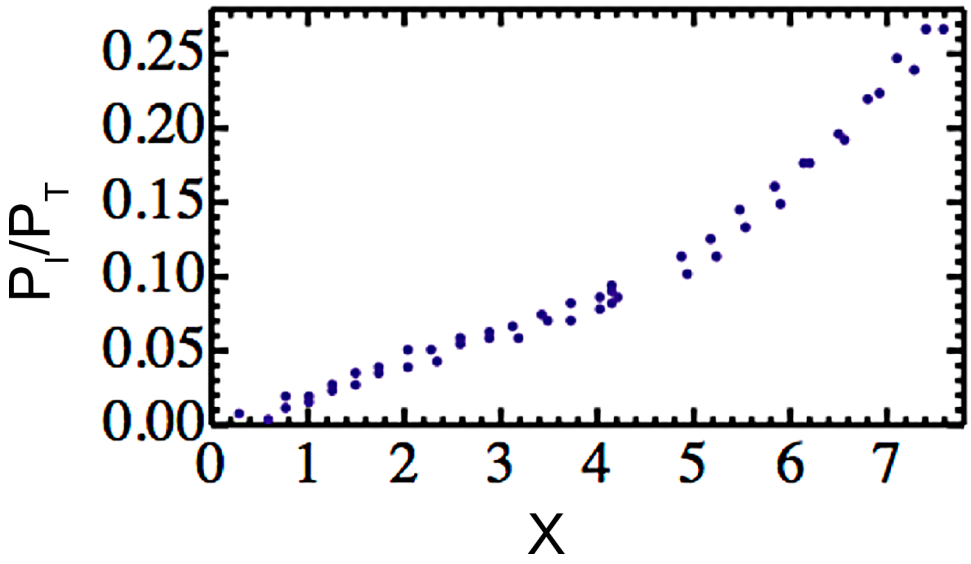

Figure 4.9: Examples of discrete changes in Fano factor at particular threshold voltage biases of tens of mV. Such changes in slope are consistent with previously reported observations [12] of inelastic electronic interactions with local vibrational modes, though in this case the junctions involve many conductance channels. The junction in this figure has a resistance of 1.1 kΩ.

a single, nearly fully transmitting channel) prepared through a mechanical break-junction approach [12]. Those kinks are clustered in bias near 17 mV, an energy scale comparable to an optical phonon in au, and attributed to electrons coupling to this mode in the atomic-scale nanowires. Moreover, those authors find a systematic relationship between the sign of the change in Fano factor, ΔF, when $V_{\rm DC}$ crosses the kink, and the total junction conductance. In contrast, our measurements show qualitatively similar kinds in junctions traversed by as many as twenty channels (based on the total conductance of the junction, which is still limited by the constriction rather than the leads), with no obvious correlation between total conductance and sign or magnitude of ΔF. This implies that such electron-vibrational modifications to the excess noise are still relevant even in many-channel junctions, with the sign and magnitude of ΔF potentially being set by the transmittance of the particular chan-

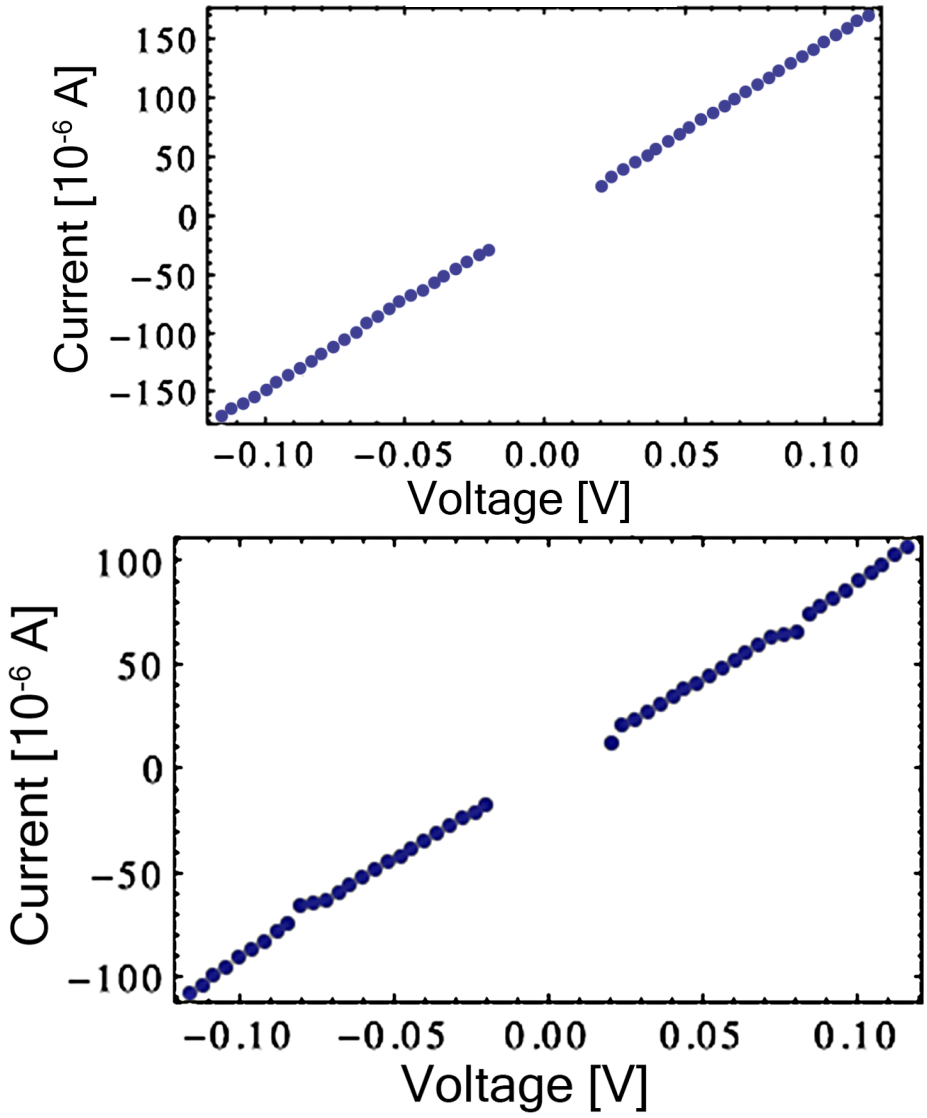

Figure 4.10: These figures show the relevant simultaneously acquired I as a function of V_{DC} data. These data do not show perceptible kinks at the voltages relevant for the changes in Fano factor, though this is not particularly surprising, given that lock-in techniques are generally necessary to resolve such features.

nel that happens to be strongly coupled to the local vibrational mode. While the variation of the kink voltage scale in our junctions is significant, the rough magnitude suggests that the inelastic mode could be due to an adsorbate, such as molecular hydrogen [61], rather

than optical phonons of the metal itself.

In addition to these kinks, we see evidence for deviations in the noise from the simple expectations of Equation (4.1) in some fraction of junctions. Figures 4.11– 4.13 show a clear example of two particular features. Figure 4.11 shows the current (strictly speaking, the change in I due to the square wave from 0 to $V_{\rm DC}$) as a function of time [AU], as $V_{\rm DC}$ is varied up and down through both polarities up to a maximum magnitude of 100 mV. At a time index of approximately 2600, there is a clear configurational change in the

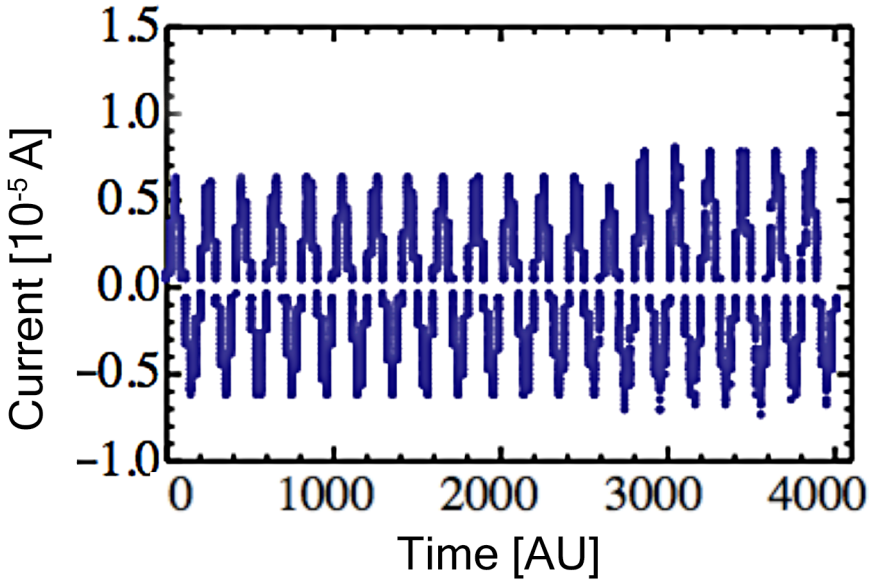

Figure 4.11: Noise asymmetry and mesoscopic sensitivity: Current as a function of time as $V_{\rm DC}$ is swept in a triangle wave between -200 mV and +200 mV, showing a stochastic transition between two junction configurations with similar conductances. Zero-bias resistance of the junction is 34 kΩ.

junction, as seen by the obvious change in I as a function of $V_{\rm DC}$. Figure 4.12 shows the corresponding P_I/P_T versus X averaged over the bias sweeps in the initial junction configuration, while Figure 4.13 shows the noise after the configurational change. In both configurations, two distinct branches are apparent, indicating that there is an asymmetry

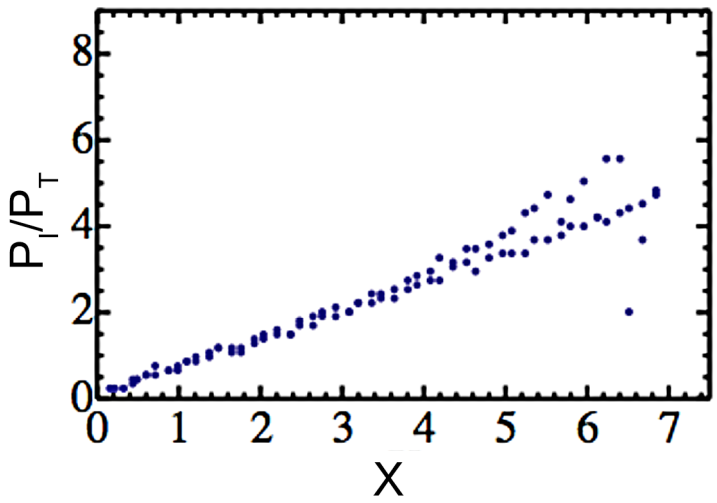

Figure 4.12: Noise asymmetry and mesoscopic sensitivity: the averaged, normalized excess noise as a function of scaled bias for the first configuration, showing two distinct branches, the upper branch with higher maximum noise corresponding to positive bias polarity.

in the noise response between the different bias polarities, with positive bias corresponding to higher inferred bias-driven noise. In twenty-eight junction configurations, we observe some distinct asymmetry in P_I/P_T versus X as a function of the polarity of $V_{\rm DC}$. This asymmetry is truly intrinsic to the particular junction configurations, confirmed by swapping the biasing circuitry and current amplifier between the source and drain electrodes. In most of these configurations, as here, the inferred P_I/P_T is smoothly nonlinear (no indication of sharp kinks) in X in at least one polarity. Note that, in this case, at negative bias polarity, the linearity of P_I/P_T with X is excellent, consistent with Equation (4.1) and a Fano factor of approximately 0.7. At positive bias polarity, there is a smooth, superlinear in X, contribution to the noise.

We find that asymmetries of this type (deviation from linear shot noise at one bias polarity) could also arise stochastically and irreversibly due to atomic-scale junction rearrange-

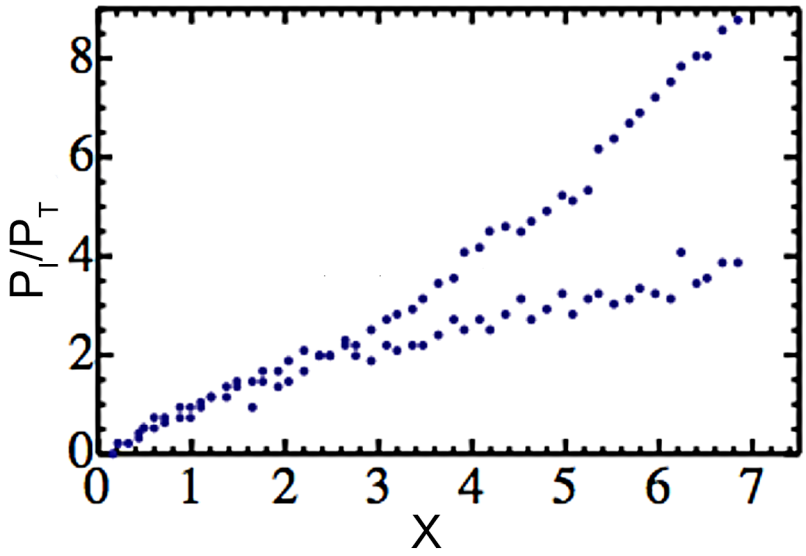

Figure 4.13: Noise asymmetry and mesoscopic sensitivity: normalized excess noise as a function of scaled bias in the second configuration, with the upper branch again corresponding to positive bias polarity.

ment at comparatively large biases ($>$150 mV), particularly in junctions with conductances of $<0.7G_0$. These changes in noise asymmetry can take place even when the accompanying change in conductance is comparatively minimal (Figure 4.14). The configurational changes in Figures 4.11– 4.13 are spontaneous examples.

After the atomic rearrangement, the zero-bias conductance increases by approximately ten percent, with a slightly higher differential conductance at positive polarity. Figure 4.15 shows the corresponding time variation of the raw lock-in amplifier reading of the RF power detector.

After this modest change in conductance, there is now a much larger asymmetry in the inferred noise, with P_I/P_T at maximum positive bias exceeding that at negative bias by more than a factor of two.

A natural source of such a nonlinearity would be flicker noise, with time-dependent

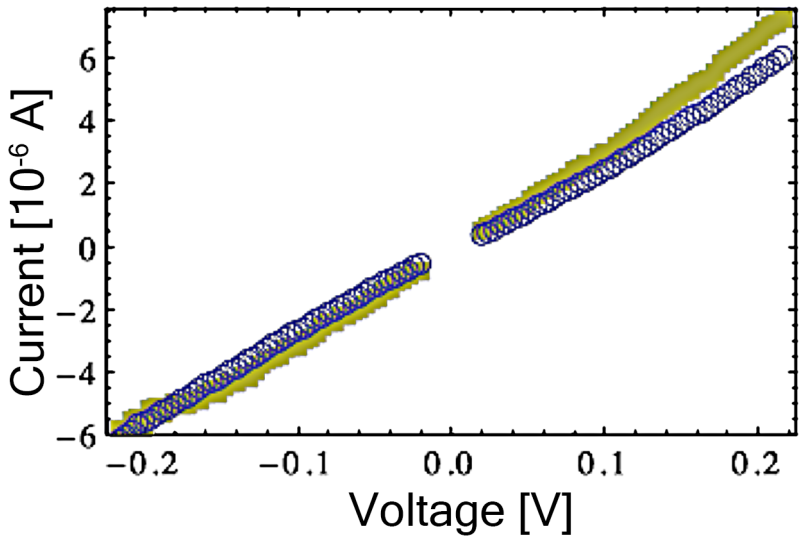

Figure 4.14: Noise asymmetry and mesoscopic sensitivity: the voltage and current of Figure 4.13 shows I as a function of $V_{\rm DC}$ before (open data marker) and after (filled data marker) the change in junction configuration. The change in noise asymmetry is considerably more dramatic.

fluctuations of the junction conductance leading to a fluctuating current; however, ordinary time-dependent conductance fluctuations should depend only on the presence and properties of fluctuators in the junction region, and do not by themselves imply an asymmetry with bias. There has been comparatively little discussion of noise processes dependent on current polarity in the literature. Experimentally, shot noise measurements in carbon nanotubes have shown asymmetry as a function of bias [62] ascribed to the same interference between conducting channels that gives rise to Fabry-Perot resonances in the conductance. Atomic-scale asymmetries in junctions have also been predicted to lead to a possible dependence of the noise on bias polarity [63] and this would be sensitive to individual atomic positions. However, given the significant nonlinearity in the noise that we observe in these asymmetric examples, we believe it more likely that some form of current-driven ionic motion tied to a flicker/conductance fluctuation mechanism is at work in our case. Time-

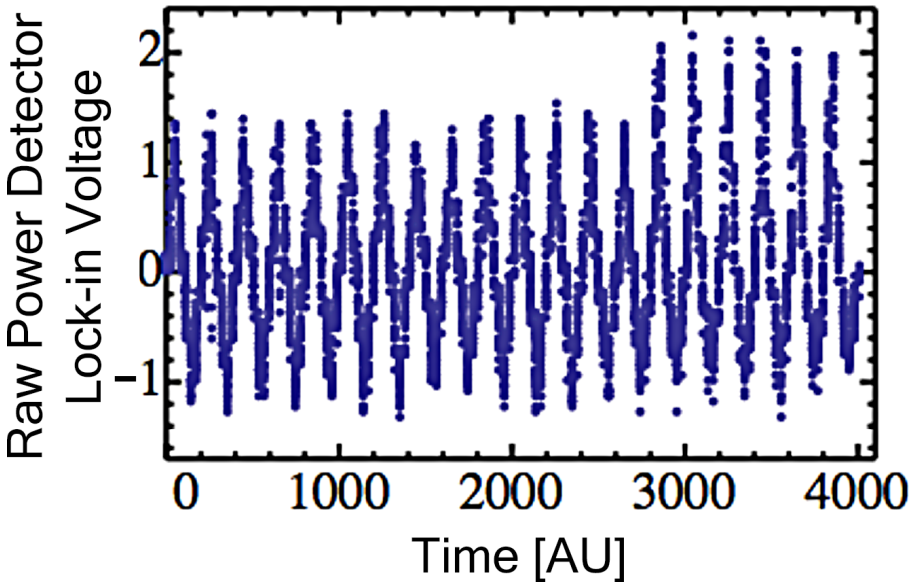

Figure 4.15: Noise asymmetry and mesoscopic sensitivity: the raw lock-in measurement of the RF power detector as a function of time, showing clearly that the second junction configuration exhibits noise that is much more asymmetric in bias than the current itself in Figure 4.11.

dependent conductance fluctuations in metal systems are believed to arise from dynamical motion of atoms or groups of atoms [1, 55].

We suggest that a likely explanation for our observed asymmetry in this contribution to the noise is local heating of ionic degrees of freedom that depends on the direction of the current. Under bias, the electronic distribution functions in the contacts near the junction are driven out of thermal equilibrium, with a population of "hot" electrons injected into the positively biased contact. Such an electronic hotspot can lead to an asymmetric heating of local ionic degrees of freedom [55] as has recently been observed experimentally [64]. An alternative mechanism could be the bias-driven runaway pumping of a locally unstable ionic vibrational mode in one of the contacts [65]. In both cases, the idea is that a localized ionic degree of freedom present in one electrode, but not the other, interacts with the local electronic distribution within an electron–electron inelastic scattering length of the

junction. The application of a bias drives the electronic distribution out of thermal equilibrium, the particular form of the local electronic distribution (and thus the effect on the ionic degree of freedom) depending on the direction of current flow. Investigations of junctions exhibiting these asymmetries, including their detailed bias dependence, are warranted, in the hopes of determining more information about the microscopic structural differences responsible.

4.2.2 Electromigrated Junction Summary

We have used high-frequency methods to examine noise in individual electromigrated nanojunctions. Many junctions show a bias dependence of the noise response consistent with conventional shot noise, Equation (4.1). However, we find two significant deviations from simple shot noise in a significant population of junction configurations, suggestive of current-driven inelastic processes involving ionic degrees of freedom. Even in junctions with comparatively many quantum channels contributing to the conduction, we observe discrete changes in the Fano factor of the noise at biases in the range of tens of mV. These are qualitatively similar to results observed [12] in atomic-scale junctions that are ascribed to inelastic processes involving local vibrational modes, suggesting that such processes are likely at work even in these larger junctions. In some junctions, we find an additional contribution to the noise with a bias dependence inconsistent with shot noise and likely associated with conductance fluctuations due to motion of ionic degrees of freedom. This additional noise can be asymmetric in bias current polarity, and is sensitive to atomic-scale rearrangements of the junction configuration. This sensitivity and the asymmetry of this noise with bias current highlight the crucial importance of understanding electronic and ionic heating at the nanoscale in future scientific investigations (for example, current noise in molecular junctions) and nanoelectronics technologies.

Chapter 5

Summary Remarks and Future Directions

A novel measuring technique was used to probe quantum shot noise characteristics in atomic scale junctions at liquid nitrogen and room temperatures. This technique utilized high-frequency, broadband RF signal measurements of square-wave biased junctions and simultaneous extraction of shot noise power and conductance measurement data at high sampling rates.

The associated electronic circuits that enabled this measurement technique were calibrated and validated using an in-situ vacuum photodiode, ensuring confidence and accuracy in measuring atomic scale junctions. Stringent, watertight EMI-mitigation techniques were also an essential part of the experimental design to further improve signal-to-noise ratio.

Junctions were created and measured at room temperature, utilizing both MCBJ and STM–BJ experimental design hardware. Shot noise power of $\sim 10^{-16}$ watts was successfully measured at room temperature in a sea of other intrinsic and extrinsic noise sources. The quantum nature of conductance and shot noise suppression was observed over junction configuration ensemble averages and was confirmed to correlate well with the Landauer model.

Lithographically created junctions were also measured, using the same measurement electronics and techniques at liquid nitrogen temperature, enabling the examination of individual junction configurations rather than ensemble averages. Nonlinearity and asymmetry were found in many of the point contacts, providing opportunities for future research.

The research findings and experimental apparatus presented in this thesis are being

leveraged in Ruoyu Chen's research [41]. Chen has shown that shot noise in the STM–BJ design, in the limit of a moderate number of Landauer channels, approaches one-third of the classical $2eI$ limit expected for a diffusive mesoscopic conductor [66, 67]. Further, the remaining excess noise when shot noise is suppressed, strongly resembles flicker noise [21]. Chen [56] found that excess noise from local junction heating seems to follow the finite temperature Landauer Equation (1.11) to a good approximation above $2G_0$.

In closing, listed below are suggested areas for additional work leveraging the techniques and findings in this thesis:

- Rapid assays of shot noise through molecules in the STM–BJ system.
- Modification of the Fano factor due to phonon coupling in molecules.
- Examination of nickel and other ferromagnetic metal junctions to observe the temperature evolution of the Kondo effect through Fano factor modification.
- Continued improvement of the shielding of the attocube to further enable quantitative study of the nonlinear and asymmetric excess noise observed in this thesis.

Appendix A

Full MCBJ Electronic Circuit Diagram

A: Amplifier Chain – A series of broadband Mini-Circuits microwave amplifiers.

B: Bandpass Filters – A series of filters that limits the bandwidth of the signal measured by the Mini-Circuits power detector C.

C: Power Detector – A Mini-Circuits ZX47–60+ logarithmic power detector/meter. For every dB of change in power at the input port, the output port changes by a fixed amount of voltage, ΔV.

D: Lock-in Amplifier – Stanford Research SR830 filters out off-frequency noise. D_1 is the lock-in for the power signal while D_2 is the lock-in amplifier for the conductance measurement.

E: Power Reading – BNC cable allowing direct measurement of the power detector.

F: DAQ – National Instruments USB BNC 4084 data acquisition board, a well-calibrated, multi-channeled analog-to-digital converter.

G: Bias Tee – Custom Pulsar microwave components BT-L46-411, passive RF components that allow high and low frequencies to be separated or combined.

H: Resistance Standard – General Radio 1433–G Decade Resistor and input amplitude of function generator, K, set to limit current to the pre-amplifier to avoid overload; an optional component for the electromigrated junction experimental design.

I: Current Pre-Amplifier – A Keithley 428-PROG trans-impedance amplifier converting current into an output voltage ranging from -10 to 10 volts.

J: MCBJ or STM–BJ – Device to make and break quantum point contacts (see Figures 2.1 and 2.2 for respective diagrams). When biased, the Au junction is the source of shot noise for this circuit.

K: Function Generator – Stanford Research DS345 programmable function generator with 50 Ω impedance; amplitude determines the bias across the device and the resistance standard, H. Voltage offset is set so square wave goes from zero volts to the programmed amplitude. Sync output of K is used as the input frequency reference of both lock-in amplifiers, D_1 and D_2.

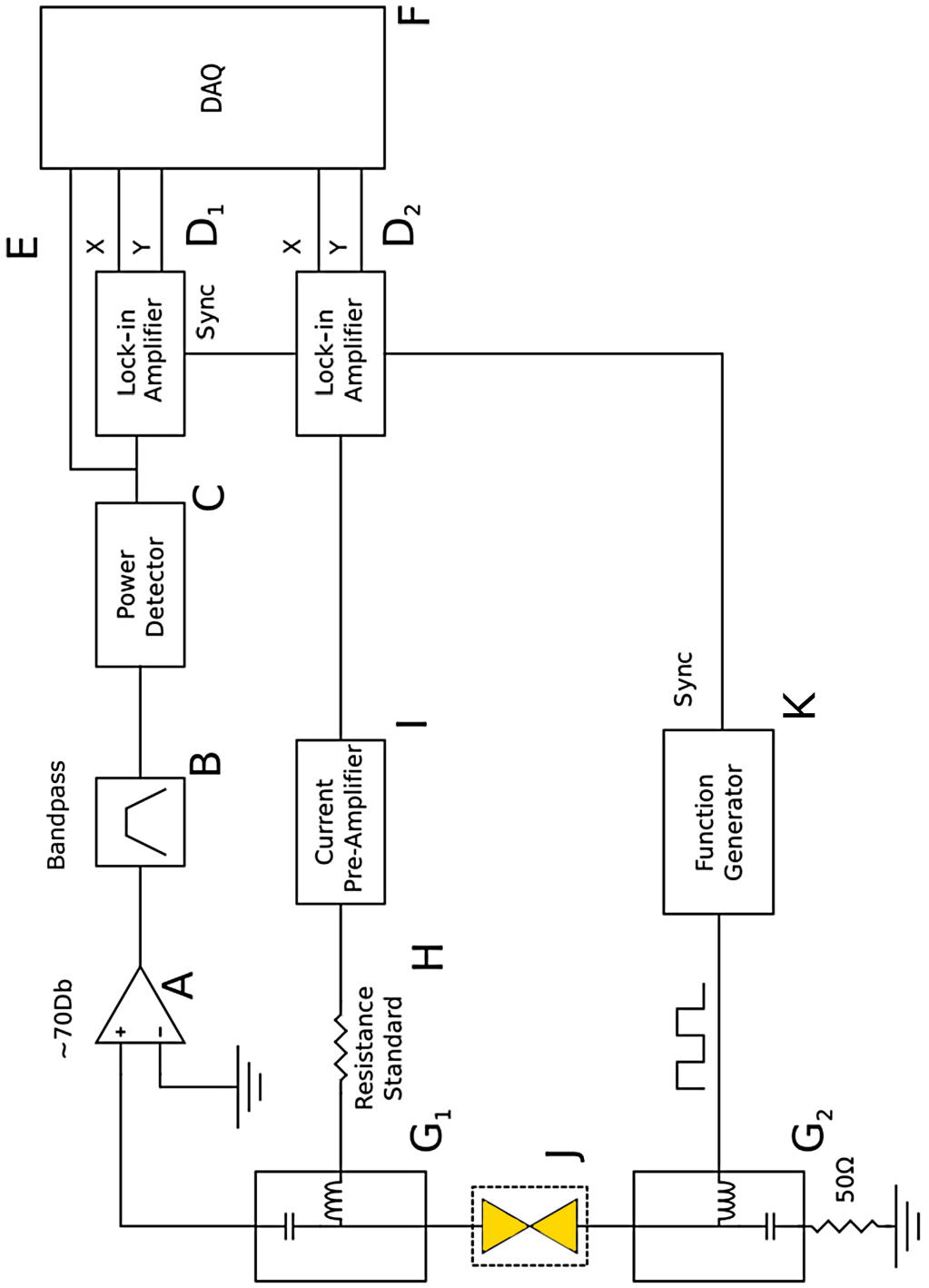

Figure A.1: Full MCBJ Electronic Circuit Diagram with detailed descriptions and part numbers.

Appendix B

Full Photodiode Electronic Circuit Diagram

A: Amplifier Chain – A series of broadband Mini-Circuits microwave amplifiers.

B: Bandpass Filters – A series of filters that limits the bandwidth of the signal measured by the Mini-Circuits power detector C.

C: Power Detector – A Mini-Circuits ZX47–60+ logarithmic power detector/meter. For every dB of change in power at the input port, the output port changes by a fixed amount of voltage, ΔV.re

D: Lock-in Amplifier – Stanford Research SR830 filters out off-frequency noise. D_1 is the lock-in for the power signal while D_2 is the lock-in amplifier for the conductance measurement.

E: Power Reading – BNC cable allowing direct measurement of the power detector.

F: DAQ – National Instruments USB BNC 4084 data acquisition board, a well-calibrated, multi-channeled, analog-to-digital converter.

G: Bias Tee – Custom Pulsar microwave components BT-L46-411, passive RF components that allow high and low frequencies to be separated or combined.

H: Resistance Standard – General Radio 1433–G Decade Resistor and input amplitude of function generator, K, set to limit current to the pre-amplifier to avoid overload; an optional component for the electromigrated junction experimental design.

I: Current pre-Amplifier – A Keithley 428-PROG trans-impedance amplifier converting current into an output voltage ranging from -10 to 10 volts.

J: Photodiode – 1p39 vacuum photodiode; the source of this circuit's shot noise.

K: Function Generator – Stanford Research DS345 programmable function generator with 50 Ω impedance; amplitude determines the bias across the device and resistance standard, H. Voltage offset is set so square wave goes from zero volts to the programmed amplitude. Sync output of K is used as the input frequency reference of both lock-in amplifiers, D_1 and D_2.

L: LED – Light-emitting diode biased with a square wave from K, used to stimulate photodiode, J.

M: -45V – Connection providing bias to the photodiode to produce a voltage difference between the photodiode's cathode and anode.

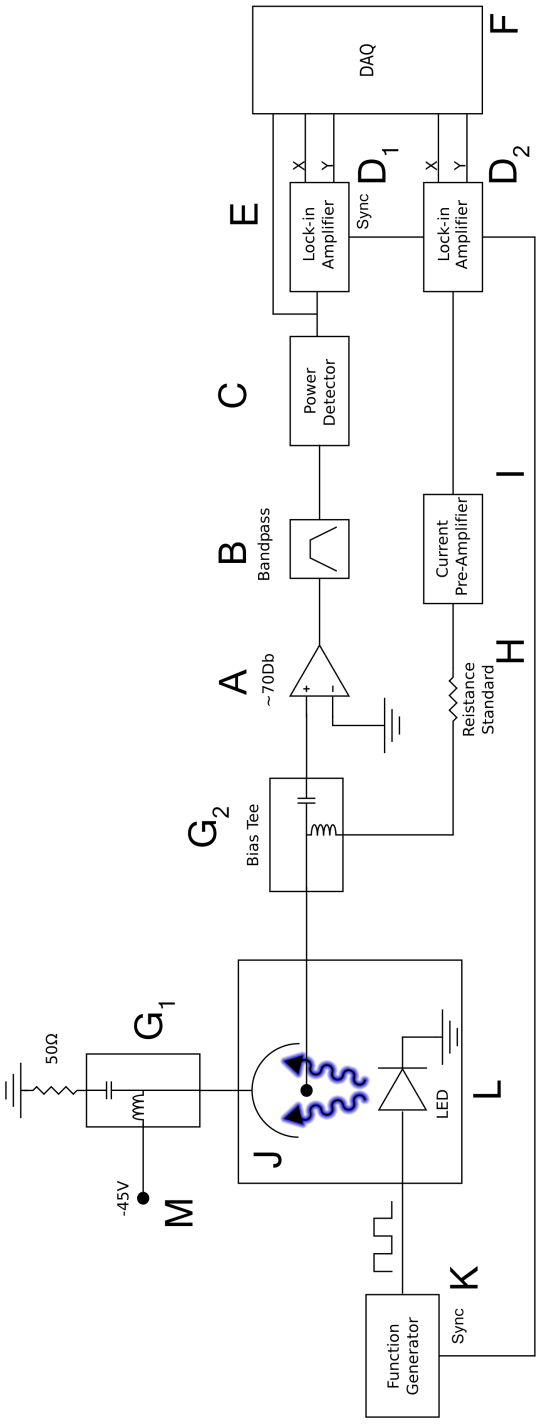

Figure B.1: Full Photodiode Electronic Circuit Diagram with detailed descriptions and part numbers.

Appendix C

Experimental Tips and Techniques

Note: There are several components to the tips and techniques below, referring to RF interconnects:

- RF cable
- Male or female connector
- Interface when connecting male to female connector
- Cable Connector Interface (referred to as CCI in this appendix)
- Connection System (when referring to all RF interconnect components as a whole)

SMA versus BNC connectors – BNC connection systems have been found to have a number of issues that did not occur with SMA connection systems. BNC connection systems are typically rated for up to 2 GHz, yet were found not practical for the 200–500 MHz high-frequency work of this research. BNC connectors too often became loose, either through heavy use or slightly mismatched sizes between male and female connectors; SMA connectors do not appear to have this size mismatch issue. A high-quality purchased BNC connection system, with proper stress relief, typically lasts for several years or more; however, the handmade connectors rarely lasted more than two years, primarily due to the CCI. Handmade BNC CCIs often have degraded quality over time, because of physical wear and tear. Sometimes, the custom BNC

CCIs would end up with an intermittent RF leak when bent/hung in a particular way, making the issue very difficult to track down. Bottom line recommendation for this type of research, as of this printing, is to use SMA connection systems.

Torque wrench for SMA connectors – Hand-tightening SMA connectors is a common practice, yet it is not recommended for critical work. The RF-shielding characteristics are not consistent with hand-tightening. Also, the SMA connector can be destroyed by continued over-tightening by hand. A torque wrench obviates these issues and its use is highly recommended.

Torque wrench for N Type connectors – N Type connectors are also easy to over-tighten. Torque wrenches for N Type connectors would obviate this issue, yet availability of N Type connector torque wrenches is limited.

N Type connectors need cleaning – N Type connectors seem to require the most maintenance in terms of cleaning, compared to those for BNC, SMA, SMB, and DMC. It is relatively easy for a small piece of grit to lodge in the N Type connector, causing high-frequency localized signal loss. I often observed this loss as a narrow dip in transmission between 1.5 and 2 GHz. The frequency of this loss would change with only slight pressure to the N Type connector, causing the loss characteristic to move across the spectrum. Active components of the experimental design would sometimes mix this higher-frequency loss down to low frequencies, interfering with the measurements used in this research. A no-lint brush/swab used with isopropyl alcohol was found to be a reasonable approach to cleaning the connector.

EMI mitigation – Faraday cage rules of thumb are far from adequate for this type of research. Using watertight shielding increased signal quality through reduced EMI and

greatly reduced the number of headaches that resulted from tracking down intermittent EMI issues.

Bibliography

[1] M. B. Weissman, "$1/f$ noise and other slow, nonexponential kinetics in condensed matter," *Reviews of Modern Physics*, vol. 60, pp. 537–571, Apr. 1988.

[2] A. Boden, "All sizes | in search of lost time | flickr - photo sharing!," June 2007. Available at http://www.flickr.com/photos/bogenfreund/556656621/sizes/o/.

[3] "1p39 photograph." Available at http://www.usbid.com/parts/1P39.

[4] D. R. Spiegel and R. J. Helmer, "Shot–noise measurements of the electron charge: An undergraduate experiment," *American Journal of Physics*, vol. 63, pp. 554–560, June 1995.

[5] J. M. van Ruitenbeek, "Conductance quantisation in metallic point contacts," *arXiv:cond-mat/9910394*, Oct. 1999.

[6] D. Mahalu, M. Reznikov, M. Heiblum, and H. Shtrikman, "Temporal correlation of electrons: Suppression of shot noise in a ballistic quantum point contact," *Physical Review Letters*, vol. 75, pp. 3340–3343, Oct. 1995.

[7] I. K. Yanson, O. I. Shklyarevskii, J. M. van Ruitenbeek, and S. Speller, "Aluminum nanowires: Influence of work hardening on conductance histograms," *Physical Review B*, vol. 77, p. 033411, Jan. 2008.

[8] H. E. van den Brom and J. M. van Ruitenbeek, "Quantum suppression of shot noise in atom–size metallic contacts," *Physical Review Letters*, vol. 82, pp. 1526–1529, Feb.

1999.

[9] J. M. van Ruitenbeek, A. Alvarez, I. Pieyro, C. Grahmann, P. Joyez, M. H. Devoret, D. Esteve, and C. Urbina, "Adjustable nanofabricated atomic size contacts," *Review of Scientific Instruments*, vol. 67, pp. 108–111, Jan. 1996.

[10] L. Venkataraman, J. E. Klare, C. Nuckolls, M. S. Hybertsen, and M. L. Steigerwald, "Dependence of single–molecule junction conductance on molecular conformation," *Nature*, vol. 442, pp. 904–907, Aug. 2006.

[11] attocube systems GR, "Low temperature probe station | high magnetic fields." Available at http://www.attocube.com/nanoSCOPY/attoCPSI.html.

[12] A. Yeyati, M. Kumar, J. van Ruitenach, and R. Avriller, "Detection of vibration–mode scattering in electronic shot noise," *Physical Review Letters*, vol. 108, Apr. 2012.

[13] P. W. Anderson, "More is different," *Science*, vol. 177, pp. 393–396, Aug. 1972. PMID: 17796623.

[14] L. Hoddeson, G. Baym, and M. Eckert, "The development of the quantum–mechanical electron theory of metals: 1928–1933," *Reviews of Modern Physics*, vol. 59, pp. 287–327, Jan. 1987.

[15] A. Sommerfeld, "Zur elektronentheorie der metalle," *Naturwissenschaften*, vol. 15, pp. 825–832, Oct. 1927.

[16] R. Brown, "A brief account of microscopical observations made on the particles contained in the pollen of plants, and on the general existence of active molecules in organic and inorganic bodies," *Edinburgh new Philosophical*, pp. 358–371, 1828.

[17] A. Einstein, “Uber die von der molekularkinetischen theorie der wrme geforderte bewegung von in ruhenden flssigkeiten suspendierten teilchen,” *Annalen der Physik*, vol. 322, pp. 549–560, 1905.

[18] “Looking back, Johnson and $1/f$ noise,” *Nature Physicsportal Lookingback*, 2006. Available at http://www.nature.com/physics/looking-back/johnson/index.html.

[19] J. B. Johnson, “Thermal agitation of electricity in conductors,” *Nature*, vol. 119, pp. 50–51, Jan. 1927.

[20] D. J. Levitin, P. Chordia, and V. Menon, “Musical rhythm spectra from Bach to Joplin obey a $1/f$ power law,” *Proceedings of the National Academy of Sciences*, vol. 109, pp. 3716–3720, Mar. 2012. PMID: 22355125.

[21] M. Calame, S. Wu, C. Schönenberger, M. Steinacher, S. Oberholzer, and Z. Wu, “Scaling of $1/f$ noise in tunable break junctions,” *Physical Review B*, vol. 78, p. 235421, Dec. 2008.

[22] J. B. Johnson, “Thermal agitation of electricity in conductors,” *Physical Review*, vol. 32, pp. 97–109, July 1928.

[23] R. Kubo, “The fluctuation–dissipation theorem,” *Reports on Progress in Physics*, vol. 29, p. 255, Jan. 1966.

[24] W. Schottky, “ber spontane stromschwankungen in verschiedenen elektrizittsleitern,” *Annalen der Physik*, vol. 362, no. 23, p. 541567, 1918.

[25] Y. M. Blanter and M. Büttiker, “Shot noise in mesoscopic conductors,” *Physics Reports*, vol. 336, pp. 1–166, Sept. 2000.

[26] D. A. Wharam, T. J. Thornton, R. Newbury, M. Pepper, H. Ahmed, J. E. F. Frost, D. G. Hasko, D. C. Peacock, D. A. Ritchie, and G. A. C. Jones, "One–dimensional transport and the quantisation of the ballistic resistance," *Journal of Physics C: Solid State Physics*, vol. 21, pp. L209–L214, Mar. 1988.

[27] B. J. van Wees, L. P. Kouwenhoven, D. van der Marel, H. von Houten, and C. W. J. Beenakker, "Quantized conductance of point contacts in a two–dimensional electron gas," *Physical Review Letters*, vol. 60, pp. 848–850, Feb. 1988.

[28] D. Glattli, L. Saminadayar, B. Etienne, A. Kumar, and Y. Jin, "Experimental test of the quantum shot noise reduction theory," *Physical Review Letters*, vol. 76, pp. 2778–2781, Apr. 1996.

[29] R. Landauer and T. Martin, "Equilibrium and shot noise in mesoscopic systems," *Physica B: Condensed Matter*, vol. 175, pp. 167–177, Dec. 1991.

[30] G. Rubio, N. Agrat, and S. Vieira, "Atomic–sized metallic contacts: Mechanical properties and electronic transport," *Physical Review Letters*, vol. 76, pp. 2302–2305, Mar. 1996.

[31] N. Agrait, A. L. Yeyati, and J. M. Van Ruitenbeek, "Quantum properties of atomic–sized conductors," *Physics Reports*, vol. 377, no. 23, pp. 81–279, 2003.

[32] J. M. Krans, C. J. Muller, I. K. Yanson, T. C. M. Govaert, R. Hesper, and J. M. van Ruitenbeek, "One–atom point contacts," *Physical Review B*, vol. 48, pp. 14721–14724, Nov. 1993.

[33] C. A. Martin, D. Ding, H. S. J. van der Zant, and J. M. van Ruitenbeek, "Lithographic mechanical break junctions for single–molecule measurements in vacuum: possibilities and limitations," *New Journal of Physics*, vol. 10, p. 065008, June 2008.

[34] G. R. Bollinger, A. L. Yeyati, E. Scheer, J. M. van Ruitenbeek, J. C. Cuevas, A. Martin-Rodero, L. Bas, C. Urbina, and N. Agraït, "The signature of chemical valence in the electrical conduction through a single–atom contact," *Nature*, vol. 394, no. 6689, pp. 154–157, 1998.

[35] Xiao, Xu, and N. J. Tao, "Measurement of single molecule conductance: benzenedithiol and benzenedimethanethiol," *Nano Letters*, vol. 4, pp. 267–271, Feb. 2004.

[36] L. Grter, F. Cheng, T. T. Heikkil, M. T. Gonzlez, F. Diederich, C. Schnenberger, and M. Calame, "Resonant tunnelling through a C60 molecular junction in a liquid environment," *Nanotechnology*, vol. 16, p. 2143, Oct. 2005.

[37] L. Venkataraman, J. E. Klare, I. W. Tam, C. Nuckolls, M. S. Hybertsen, and M. L. Steigerwald, "Single–molecule circuits with well–defined molecular conductance," *Nano letters*, vol. 6, no. 3, pp. 458–462, 2006.

[38] F. Chen, X. Li, J. Hihath, Z. Huang, and N. Tao, "Effect of anchoring groups on single–molecule conductance: comparative study of thiol–, amine–, and carboxylic–acid–terminated molecules," *Journal of the American Chemical Society*, vol. 128, pp. 15874–15881, Dec. 2006.

[39] Y. S. Park, A. C. Whalley, M. Kamenetska, M. L. Steigerwald, M. S. Hybertsen, C. Nuckolls, and L. Venkataraman, "Contact chemistry and single–molecule conductance: a comparison of phosphines, methyl sulfides, and amines," *Journal of the American Chemical Society*, vol. 129, pp. 15768–15769, Dec. 2007.

[40] T. Pan, X. You, and C. Lim, "Evaluation of floor vibration in a biotechnology laboratory caused by human walking," *Journal of Performance of Constructed Facilities*,

vol. 22, no. 3, pp. 122–130, 2008.

[41] R. Chen, P. J. Wheeler, and D. Natelson, "Excess noise in STM–style break junctions at room temperature," *Physical Review B*, vol. 85, p. 235455, June 2012.

[42] H. Park, A. K. L. Lim, A. P. Alivisatos, J. Park, and P. L. McEuen, "Fabrication of metallic electrodes with nanometer separation by electromigration," *Applied Physics Letters*, vol. 75, pp. 301–303, July 1999.

[43] D. R. Strachan, D. E. Smith, D. E. Johnston, T.-H. Park, M. J. Therien, D. A. Bonnell, and A. T. Johnson, "Controlled fabrication of nanogaps in ambient environment for molecular electronics," *Applied Physics Letters*, vol. 86, p. 043109, Jan. 2005.

[44] Mini-Circuits, "Coaxial Power Detector - ZX47-60+ Data Sheet." Available at http://www.minicircuits.com/pdfs/ZX47-60+.pdf.

[45] I. K. Yanson, O. I. Shklyarevskii, S. Csonka, H. van Kempen, S. Speller, A. I. Yanson, and J. M. van Ruitenbeek, "Atomic–size oscillations in conductance histograms for gold nanowires and the influence of work hardening," *Physical Review Letters*, vol. 95, p. 256806, Dec. 2005.

[46] Y.-C. Chen, M. Zwolak, and M. Di Ventra, "Local heating in nanoscale conductors," *Nano Letters*, vol. 3, pp. 1691–1694, 2003.

[47] Y.-C. Chen and M. Di Ventra, "Effect of electron–phonon scattering on shot noise in nanoscale junctions," *Physical Review Letters*, vol. 95, p. 166802, Oct. 2005.

[48] A. Mitra, I. Aleiner, and A. J. Millis, "Phonon effects in molecular transistors:Quantal and classical treatment," *Physics Review B*, vol. 69, p. 245302, June 2004.

[49] J. Koch and F. von Oppen, "Franck–Condon blockade and giant Fano factors in transport through single molecules," *Physical Review Letters*, vol. 94, p. 206804, May 2005.

[50] E. Sela, Y. Oreg, F. von Oppen, and J. Koch, "Fractional shot noise in the Kondo regime," *Physical Review Letters*, vol. 97, p. 086601, Aug. 2006.

[51] P. Dutta and P. M. Horn, "Low–frequency fluctuations in solids: $1/f$ noise," *Reviews of Modern Physics*, vol. 53, pp. 497–516, July 1981.

[52] B. Ludoph, M. H. Devoret, D. Esteve, C. Urbina, and J. M. van Ruitenbeek, "Evidence for saturation of channel transmission from conductance fluctuations in atomic–size point contacts," *Physical Review Letters*, vol. 82, pp. 1530–1533, Feb. 1999.

[53] M. Tsutsui, M. Taniguchi, and T. Kawai, "Local heating in Metal–Molecule–Metal junctions," *Nano Letters*, vol. 8, pp. 3293–3297, Oct. 2008.

[54] D. R. Ward, N. J. Halas, and D. Natelson, "Localized heating in nanoscale Pt constrictions measured using blackbody radiation emission," *Applied Physics Letters*, vol. 93, p. 213108, Nov. 2008.

[55] R. D'Agosta, N. Sai, and M. Di Ventra, "Local electron heating in nanoscale conductors," *Nano letters*, vol. 6, pp. 2935–2938, Dec. 2006.

[56] R. Chen, P. J. Wheeler, M. Di Ventra, and D. Natelson, "Electron heating in atomic–scale Au break junctions," *arXiv:1306.6639 [cond-mat]*, June 2013.

[57] T. L. Schmidt and A. Komnik, "Charge transfer statistics of a molecular quantum dot with a vibrational degree of freedom," *Physical Review B*, vol. 80, p. 41307, July 2009.

[58] R. Avriller and A. Levy Yeyati, "Electron–phonon interaction and full counting statistics in molecular junctions," *Physical Review B*, vol. 80, p. 41309, July 2009.

[59] F. Haupt, T. Novotný, and W. Belzig, "Phonon–assisted current noise in molecular junctions," *Physical Review Letters*, vol. 103, p. 136601, Mar. 2009.

[60] T. Novotný, F. Haupt, and W. Belzig, "Nonequilibrium phonon backaction on the current noise in atomic–sized junctions," *Physical Review B*, vol. 84, p. 113107, Sept. 2011.

[61] D. Djukic, K. S. Thygesen, C. Untiedt, R. H. M. Smit, K. W. Jacobsen, and J. M. van Ruitenbeek, "Stretching dependence of the vibration modes of a single–molecule Pt-H_2-Pt bridge," *Physical Review B*, vol. 71, p. 161402, Apr. 2005.

[62] F. Wu, P. Queipo, A. Nasibulin, T. Tsuneta, T. H. Wang, E. Kauppinen, and P. J. Hakonen, "Shot noise with interaction effects in single–walled carbon nanotubes," *Physical Review Letters*, vol. 99, p. 156803, Oct. 2007.

[63] J. Yao, Y.-C. Chen, M. Di Ventra, and Z. Q. Yang, "Effect of atomic geometry on shot noise in aluminum quantum point contacts," *Physical Review B*, vol. 73, p. 233407, June 2006.

[64] M. Taniguchi, T. Kawai, and M. Tsutsui, "Unsymmetrical hot electron heating in quasi–ballistic nanocontacts," *Scientific Reports*, vol. 2, Jan. 2012.

[65] J.-T. Lu, M. Brandbyge, and P. Hedegrd, "Blowing the fuse: Berrys phase and runaway vibrations in molecular conductors," *Nano Letters*, vol. 10, pp. 1657–1663, May 2010.

[66] K. E. Nagaev, "On the shot noise in dirty metal contacts," *Physics Letters A*, vol. 169, pp. 103–107, Sept. 1992.

[67] M. J. M. de Jong and C. W. J. Beenakker, "Semiclassical theory of shot–noise suppression," *Physical Review B*, vol. 51, pp. 16867–16870, June 1995.